POLITECNICO DI TORINO

Master of Science's Degree in Biomedical Engineering

Reconstructing trajectory during an upper limb functional task: A single IMU optimization approach

Supervisors
Prof. Marco Knaflitz
Dr. Marco Ghislieri
Ing. Gregorio Dotti

Candidate
Quattrocchio Simone

March 2025

Contents

Abstract

This thesis examines trajectory reconstruction during a drinking task, a common rehabilitation exercise used to assess upper limb functionality, using a single inertial unit (IMU) worn on the wrist. Compared to other human motion capture methods, inertial measurements are a cheaper and more ergonomic alternative, but they are prone to noise and drift errors that by accumulating over time, lead to an inaccurate estimation. The aim of this work is to develop an optimization-based method to enhance trajectory reconstruction accuracy when using a single wrist-mounted IMU within a structured protocol. The proposed method is validated against a stereophotogrammetric gold standard. This approach has potential applications in telerehabilitation by enabling objective clinical assessments of functional tasks with minimal setup, making it accessible for remote use by non-experts.

To evaluate IMU performance, an initial analysis was conducted on uniaxial movements using a double integration approach. For this purpose, a custom-built workbench was designed, featuring a sliding cart on which the IMU was mounted to test controlled slide distance trajectory reconstruction. A simple double integration approach was applied to assess errors when integration was performed directly without precautions. To identify start and end points for integration, a template-matching method was developed, averaging multiple slide trials to generate a reference template for precise segmentation. Results indicate an absolute error of approximately 1 $\pm$ 0.5 cm per axis over a 15 cm slide, corresponding to 6% of the total movement

Following this preliminary analysis, the same IMU was then tested on a drinking task (R2G) involving 11 subjects. Trajectories were reconstructed using direct double integration and the zero-velocity update (ZUPT) technique. A statistical algorithm, DynAMoS, was employed to detect static periods, which were then used to apply ZUPT. Additionally, an optimization method was developed to refine trajectory estimation based on expected movement characteristics.

Results indicate that applying ZUPT to the dynamic phases identified by DynAMoS reduces trajectory reconstruction mean absolute errors compared to double integration by more than 40% of the range of motion along each axis in most subjects. However, an error of approximately 20% of range of motion still remains relative to the gold standard. After optimization, the trajectory reconstruction mean absolute error improves to less than 2 cm on all axes for most subjects, with a normalized error relative to the movement's range of motion of less than 10% for x-axis and around 5% on other axes.

These findings suggest that accurate trajectory estimation can be achieved using minimal anthropometric data and a single IMU, with errors remaining below 10% of the range of motion (ROM). However, this error is higher compared to more complex approaches, such as multi-IMU kinematic models, which achieve errors in the 1–2% range.

Despite this limitation, the proposed approach represents a viable solution for telerehabilitation due to its ease of setup and minimal measurement requirements. Future

research should explore its effectiveness in clinical populations, particularly in patients with motor impairments. Additionally, incorporating new functional cost terms may further reduce errors and improve overall accuracy.

Chapter 1

Introduction

1.1 Daily living activities

Activities of daily living (ADLs) is a term that refers to the collective set of skills required for independence such as eating, bathing, and mobility. ADLs are used as indicator of functionality and overall well being of a person, and their damage results in dependence on other people and/or need of support devices. The loss of these skills result in admission to a nursing home, change in living routine, hospitalization and paid home care; by monitoring ADLs functionality trend, is possible to predict the likelihood of a person's ability to meet personal goals and sustain independent living [1]. A research of United States National Health Interview Survey shows that in 2011, of 20.7% of adults aged 85 or older, 7% of those aged 75 to 84, and 3.4% of those aged 65 to 74 needed help with ADLs [2].

One of the most common leading cause of disability worldwide is stroke; leading to impairment in 80% of cases, that starts first, with an abnormal activity of the upper limb (muscle weakness, contractures, changes in muscle tone, joint laxity or impaired motor control) and can results in reduction of quality of life [3].

Upper limb mobility is essential in everyday ADLs and patients affected a by stroke have it compromised in 85% of cases [4]. The common practice in clinics is to assert the state of rehabilitation by using subjective scores that, although easy to understand and fast to be evaluated, may vary from clinician to clinician. Also, subtle change can be difficult to observe clearly and it can pass unnoticed. The success of a rehabilitation depends on an iterative process made up of impairment assessments, goal definition, intervention, and progress evaluation. Therefore, it is important to develop accurate clinical assessments that reduce the clinical subjectivity and give proper motor rehabilitation treatments [5].

The difficulty of this task comes from two reasons:

- impairment are dynamic and change over time during rehabilitation
- the patient can present comorbidities

The new methods and models used to treat patients should also consider the International Classification of Functioning Disability and Health (ICF), conceived by the World Health Organization in 2001, a framework designed to consider multiple aspects of disability such as biological, psychological, and social aspects of health, and consider multiple dimensions of human functioning and their interaction with contextual factors[6].

In this context, instrumental tests and measures can be combined with clinical evaluation to present a more clear picture of the overall state of the patient and provide a more adequate rehabilitation.

1.2 Telerehabilitation

Given the critical importance of accurately assessing and addressing impairments in ADLs, innovative technologies and related telemedicine solutions have emerged as innovative tools in healthcare. The limitations of traditional, clinician-dependent evaluation methods further highlight the need for remote monitoring and rehabilitation solutions that maintain continuity of care while reducing the burden on healthcare systems.

Due to the increasing number of the aging population, the time available to medical personnel for assistance will only get shorter. The aging population in Europe is on an increasing trend of growth. A recent study has estimated that by 2070, people with long-term care needs will increase from 11.6% in 2020 to 14.1%. The number of people in this group with 50 or more years, who will need long-term care needs, is expected to increase up to 21% from 2020 to the same year [7].

The median age has increased by 2.3 years from 2013 to 2023, reaching 44.5 years as seen in fig. 1.1. The old-age dependency ratio, described as the ratio of the number of elderly people (65+ years) with working age (15-64), has raised by 5.7% from 2013, when it was at 27.7%, [8], as seen in fig. 1.2. Aging of the population is also associated with difficulty in performing ADLs and the number of elderly people in Europe able in carrying out personal or household activities without assistance is only around 50%, according to a statistic of 2019 [9]; as seen in fig. 1.3, Italy is in line with this European value.

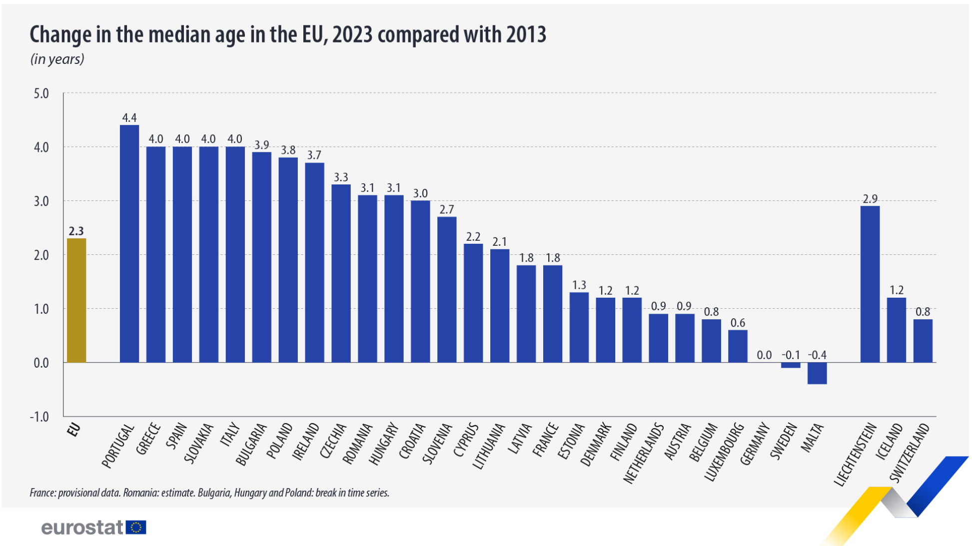

Figure 1.1: Change in median age in Europe from 2013 to 2023. Image source [8]

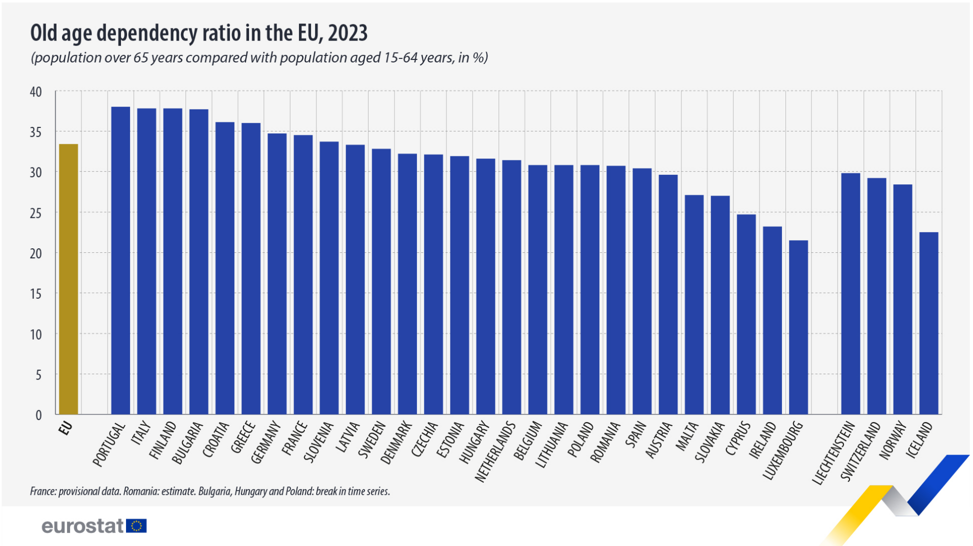

Figure 1.2: Old age dependency rate in Europe (2023). Image source [8]

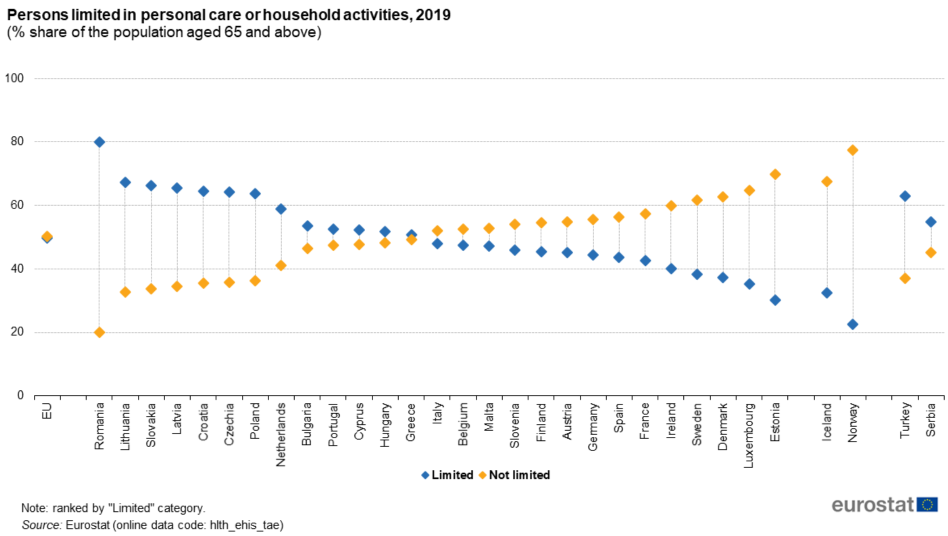

Figure 1.3: Person's limitation in personal care or household activities (2019); in blue limited, in yellow not limited. Image source [9]

Moreover, in this contextual frame of an ever-increasing aging population in Europe, with the associated need for personal care, telerehabilitation, defined as the group of activities that constitute a rehabilitative intervention delivered at a distance has become increasingly essential. This modality has grown in importance due to its ability to improve access to care, reduce geographic and financial barriers, and maintain continuity of treatment for patients unable to attend in-person sessions.

Especially after covid 19 pandemic, the necessity of implement treatments more focused on single patient's needs instead of looking only at disease related treatments has become more important. Doctor visits during this time, dropped by up to 60%, while digital remote care options as telemedicine and digital health apps grew [10].

Telerehabilitation has demonstrated potential in reducing healthcare costs. For instance, a study estimated that telehealth could save between $147.4 to $186.1 per visit in indirect costs [11]. Through telerehabilitation platforms, patients can access guided exercises, video demonstrations, and real-time feedback from therapists through video conferencing. Advanced tools like motion sensors, wearable devices, and interactive software can track progress and ensure the accuracy of movements. Virtual reality and gamified platforms further enhance engagement and adherence, making therapy more interactive and motivating.

Upper limb rehabilitation is a vital component of recovery for individuals with injuries, neurological conditions (e.g., stroke), or musculoskeletal disorders. Telemedicine has transformed this field by enabling custom and patient-centered therapy programs to be conducted at home under remote supervision. By integrating telemedicine into upper limb rehabilitation, healthcare providers can deliver high-quality, personalized care that promotes functional recovery, reduces the burden of travel, and fosters patient independence, while ensuring consistent monitoring and support. This approach represents a significant step forward in achieving equitable and effective rehabilitation outcomes.

This new approach of applying healthcare intervention, has also been demonstrated to be a growing market. It was estimated that the global market size consisted in $5.32 billion and is projected to grow at a compound annual growth rate (CAGR) of 13.2% from 2025 to 2030, reaching approximately $11.81 billion by 2030 [12], as shown in fig. 1.4.

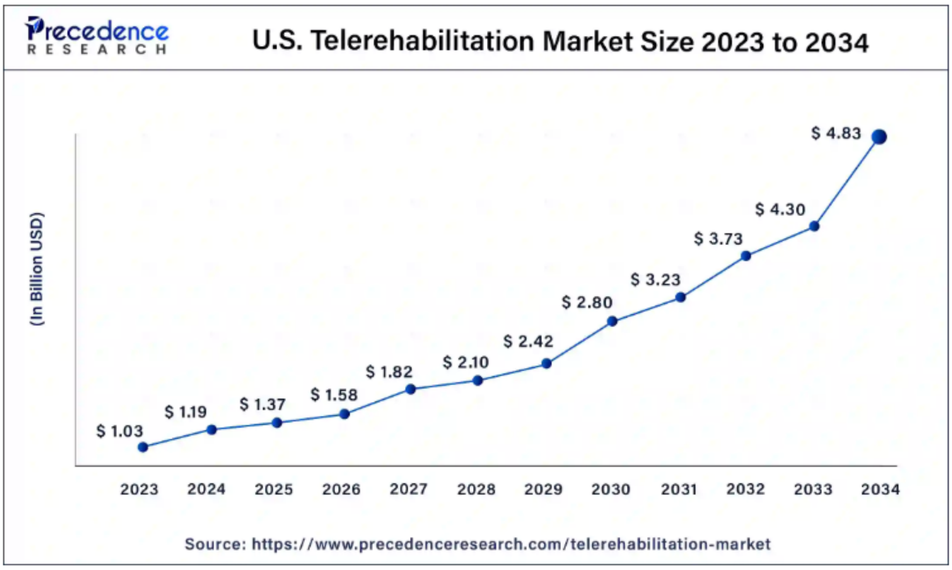

Figure 1.4: U.S. telerehabilitation market growth from 2023 to 2024. Image source.[12]

1.3 Human motion analysis methods

As discussed previously, human movement, necessary for ADLs, is essential for the overall quality of life. It improves both physical and mental health, provide independence and overall well-being [13]. It has been shown how physical activity contributes to reducing blood sugar levels and the risks in developing cardiovascular diseases [14]. Over the years many methods of analyzing human motion have been developed, each one with different characteristic and trade-off. Motion analysis has been widely utilized in clinical settings, not only for diagnosing a range of conditions, but also for creating treatment plans adaptable to patients. Another application is in judging the performance of medical devices such as orthopedic implants and rehabilitation tools. Consequently, the advancement of precise and user-friendly motion analysis methods will significantly enhance orthopedic surgeries, rehabilitation practices, precision medicine, and research in medical engineering [15], [16]. In this section are explored the physical principles, trade off and the working aspects of two of the most commonly used methods for motion analysis.

1.3.1 Stereophotogrammetry

One of the most widely used methods is stereophotogrammetry, which involves the use of reflective markers and multiple synchronized cameras operating within specific electromagnetic spectrum bandwidths (typically visible light or infrared). By using the principle of triangulation [17], it is possible to reconstruct the 3D position of each reflective marker by using the information from at least two other perspectives. Each camera, at each time sample, emits a pulse wave within a specific bandwidth and can detect, if not occluded, the reflection from the marker. By doing so, the 2D projection of the marker is recorded for each camera. Using triangulation, the 3D position of the marker can be estimated.

Given a 3D point Q in the absolute coordinate system, represented as $[x, y, z]$, its projection onto the 2D image plane can be expressed as:

$$Q' = [u, v],$$

where Q' represents the coordinates on the image plane 1.5 .

.

To express the point O in homogeneous coordinates, we write:

$$O' = [x, y, z, 1].$$

Using the perspective projection, the relationship between O' and Q' is represented as:

$$O' = P \cdot Q',$$

where P is a 3×4 projection matrix [17]. The projection matrix P can be decomposed into two main components: extrinsic parameters $(R \cdot t)$ and intrinsic parameters C.

$$P = R \cdot t \cdot C \tag{1.1}$$

The extrinsic parameters describe the camera's position and orientation in the absolute coordinate system. Here, R is a 3×3 rotation matrix that aligns the absolute coordinate axes with the camera's axes, while t is the 3×1 translation vector describing the displacement from the origin of the absolute coordinate system to the camera's origin.

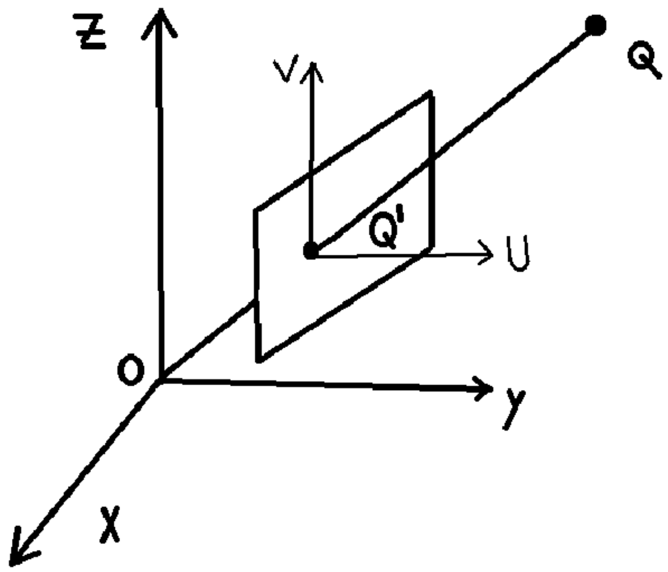

Figure 1.5: Schematic representation of projection of a point (Q) into projection plane (VU) with global reference system (XYZ).

The intrinsic parameters are contained in the 3×3 matrix C, which defines the internal properties of the camera. So, it is possible to compute up to a scale factor the 2D-3D transformation by knowing the projection matrix P. Intrinsic and extrinsic parameters can be found by calibrating the cameras. This is done by using a calibration system, consisting in a certain number of markers placed at known relative distances. With the calibration phase each camera first computes P from a set of markers with known 3D positions, and the relative projection on image plane, then decomposes P into C, R and t [18].

Stereophotogrammetry method, having high resolution for both kinematics and spatio-temporal parameters, is often used as gold standard for human motion analysis. It is however expensive, due to high cost of both instrumentation and software, requires time to be calibrated, trained personnel, and acquisition set up available only in laboratories; for these reasons its use in telemedicine can be quite difficult and more wearable and cost-effective systems, like IMUs, are often preferred in applications such as sports science and rehabilitation.

1.3.2 Inertial measurements

Sensors for motion analysis can also be based on magneto inertial technology, by exploiting MEMS technology(Micro Electro-Mechanical Systems) to measure angular velocity, acceleration and magnetic field. MIMUs (Magneto-Inertial Measurements Units) consists of a triaxial gyroscope, a triaxial accelerometer and a triaxial magnetometer, that measure the angular velocity, the linear acceleration and the magnetic field within the sensor's reference system, respectively. These devices present optimal features to be employed in telemedicine, thanks to their high wearability, cost-effectiveness and ergonomics.

The angular velocity is measured by the gyroscope by exploiting the Coriolis effect, which correlates the apparent force exerted on the gyroscope in vibration, its mass with the angular velocity; by measuring the force is possible to compute the angular velocity

(1.2).

$$\vec{F_c} = -2m(\vec{\omega} \times \vec{v}) \tag{1.2}$$

Specifically, the gyroscope produces the apparent force with a vibrating framework (vibrating mass) and when the sensor is rotated around the perpendicular axis on which the vibrating mass is moving, an apparent force is produced on the axis found from the cross-product of the vibrating axis and the rotating axis [19]. This force can be measured by means of piezoelectric or capacitive sensors and from there, the angular velocity is computed by inverting (1.2).

The accelerometer computes the linear acceleration by means of the Newton's second law, which states that a object undergoes an acceleration proportional to the sum of forces exerted on it and inversely proportional to its mass (1.3).

$$\vec{F} = m\vec{a} \tag{1.3}$$

An accelerometer can be modeled as a mass-damper-spring system fig. 1.6; if the framework moves, an elastic force will bring it back to its starting position through an elastic force (Hooke's law) (1.4). At the same time, inertial force caused by (1.3) tend to oppose the movement

$$\vec{F} = -k\vec{x} \tag{1.4}$$

The damper slow the movement through (1.5)

$$\vec{F_d} = -c\vec{v} \tag{1.5}$$

The system can be described with equation (1.6)

$$m\ddot{x}(t) + c\dot{x}(t) + kx(t) = F(t), \tag{1.6}$$

where m is the mass, c is the damping coefficient, k is the spring constant, $x(t)$ is the displacement, and $F(t)$ is the external force applied. By using Laplace transform

$$ms^2X(s) + csX(s) + kX(s) = F(s), \tag{1.7}$$

where $X(s)$ and $F(s)$ are the Laplace transforms of $x(t)$ and $F(t)$, respectively. Rearranging to solve for $X(s)$, we get: (1.8).

$$X(s) = \frac{F(s)}{ms^2 + cs + k}. \tag{1.8}$$

By measuring through piezoresistors or capacitors the displacement x of the mass, and inverting (1.8) it is possible to obtain the inertial force which causes the acceleration. The accelerometer measure the proper linear acceleration as the proper acceleration on the sensor minus the gravity acceleration.

$$a_{\text{measured}} = a_{\text{proper}} - g$$

Thus, in static conditions the accelerometer work as an inclinometer, measuring only the gravity vector decomposed along each accelerometer axis, in free fall a null acceleration is measured. [20]

The magnetometer operates by measuring the local magnetic field using the Hall effect, which occurs when a voltage is generated across an electrical conductor that is transverse

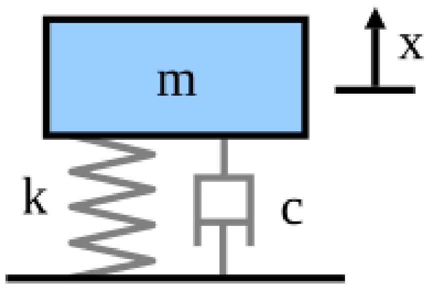

Figure 1.6: Schematic representation of spring-dumper-mass system.

to both the current flowing through it and the applied magnetic field perpendicular to the current. In ideal conditions, only the Heart's magnetic field would be registered and so the magnetometer would work as a compass [21].

Each of these sensors can alone compute the position of the sensor within the sensor's reference system; for the accelerometer by double integrating the acceleration after gravity removal, for the gyroscope by integrating the angular velocity to find the angular displacement and magnetometer by confronting the heading information of the output with the Heart local magnetic field. However, every one of them has different and specific problems, that are not easily solvable, so typically, sensor fusion algorithm is used to improve performance [22].

Gyroscope suffers from drift error caused by internal bias, which accumulates over time. This means that without countermeasures a static acquisition would cumulate in angular velocity measurements, leading to the estimation of a rotation. This can be partially solved by acquiring static trials for each axis and removing the mean value, however the drift is also temperature related, and so the device must be let warm up before acquisition. Other noise sources are random bias fluctuations and random white noise. Random bias fluctuations lead to unpredictable shifts in the sensor's output, while white noise introduces random measurement errors [19][23].

The accelerometer also suffer from drift error, because by double integrating acceleration, after having removed gravity vector, is possible to find position. However even smaller errors on acceleration propagate and accumulate over time resulting in larger errors [20], [23].

Magnetometer is sensible to other electromagnetic interferences, when a noise source is near the sensor the local magnetic field is distorted and thus accuracy decreases. It is possible to distinguish two sources of magnetic noise: soft iron and hard iron. The first one are materials that create magnetic fields in response to external fields, the second are ferromagnetic materials with permanent magnetic fields [21].

1.4 Estimating position from inertial data

Inertial sensors, in the last decade, have been explored as solution for different fields of telemedicine (orthopedic, neurological, physical medicine rehabilitative and occupational) thanks to their high wearability, inexpensiveness and non-invasive nature [24]. A review has recently suggested that they can be used as a way to assert execution of ADL for upper limb movement [25]. As discussed in 1.3.2, MIMUs are valid sensors in this field and have unique traits that make them suitable for upper limb telerehabilitation, they however, present some challenges in the processing of the signals; errors such drifts and non sistemic errors could be difficult to compensate if not used correctly. They can provide an objective measurement unlike commonly used assessment metrics and score as the Fugl-MeyerAssessment(FMA) [26], or the Box and Block Test (BBT) [27] , which, although being efficient and reliable, lack in objectivity and repeatability. One way to evaluate objectively the quality of the movement is through trajectory estimation; that means describing the displacement of the sensor/sensors in each direction over the time in the global reference system. Here are reviewed some notable methods used to estimate trajectory using inertial data.

1.4.1 Double integration from accelerometer data with boundaries conditions

The simplest way of estimating displacement from MIMU is by first aligning the reference system, removing gravity vector and then, double integrating corrected accelerations through time. Although straightforward, this method is prone to drift, caused by random noise and it propagates over time time, resulting in final large errors. This method without any precautions is not reliable if not for low speed and at most 1-2 seconds. One way to improve trajectory estimation is by using a Zero Velocity Update (ZUPT) approach, where static phases during the task are detected, and drift is compensated by setting the velocity to zero in those segments. This approach is widely used in gait analysis due to the repeatability of gait patterns and the presence of static phases, making it highly effective. For instance, in [28], a study using a foot-mounted IMU compares three zero-velocity detection methods: acceleration-moving variance detector, acceleration-magnitude detector, and angular rate energy detector. Among these, the angular rate energy detector exhibits the best performance, under controlled conditions, with precision achieved within a few centimeters per step. Experimental results indicate that the angular rate energy detector achieves a detection rate of approximately 98% with a false alarm rate below 5%. The variance-based detector follows closely with a detection rate of around 96% and a slightly higher false alarm rate of 6%. The best precision recorded is within 3-5 cm per step under controlled conditions.

In Bai, [29], it is instead used a ZUPT method in upper limb rehabilitation with single IMU on wrist, during an evaluation test (nine hole peg test). By definition of the protocol of the test, the static position are present and in this case are found by using a double threshold strategy based on short time signal energy and zero crossing rates. The gyroscope data, due to being more sensitive in change of orientation, is used to calculate short time energy as summation of the sample signal over four samples window, then zero crossing rate function is found by difference of the sign evaluation of contiguous window. By setting three thresholds, based on trial and error, is possible to detect the zero points, locate the maxima of the motion while eliminating the effect of noise. In this case, trajectory is improved by reducing position errors from several meters to 0.8% of the total movement distance. The same article propose also a kinematic model with four inertial sensors placed on the shoulder, upper arm, forearm, and hand to track upper limb movement. It constructs a multi-linked skeletal representation of the arm, treating each segment as a rigid body. The model estimates joint positions by combining sensor-measured orientations with known segment lengths, using rotation matrices to transform local sensor data into a global reference frame. This approach enables accurate tracking of upper limb motion, with errors as low as 0.1 cm over a 10 cm movement range. Another ZUPT approach applied in gait analysis, is proposed by Ayub et al. [30], where various features of the accelerometer signal from IMU on a phone are confronted. Step detection is done with two methods, zero crossing and moving variance detector, the first consists in detecting the instants in which the acceleration change sign, the second compute local mean acceleration for each sample, followed by the application of a moving variance filter to highlight foot activity. A variance threshold is then used to detect steps, with a step being identified when the variance exceeds a certain level. Out of these, zero crossing detector is more robust than moving variance step detection, with error in detection under 3%. In [31], the strategy for locating static/quasi static transient is by considering the absence/presence of the natural frequencies, that in a mechanical system represent vibrations. A new feature is calculate by summing the power spectral density in small window for each axis. By using machine learning, for example logistic regression is possible to calculate a threshold to apply to this feature and find the static period. Drift compensation improves up to 50% were shown in the stationary conditions.

Other methods relies on denoising the estimated trajectory after double integration for removing low frequency bias; for example in [32], are shown two methods. The first uses a wavelet transform to reduce noise by decomposing the signal in two parts iteratively in approximation coefficients and detail coefficients, so that is possible to reconstruct the low frequency trend with only some components. The second uses approach uses for the same purposes an high pass filter (cut-off frequency of 0.3Hz), since the source of error can be due to orientation error in the algorithm when removing the linear acceleration in order to remove gravity. Using these methods, errors of 0.5 ± 1.65 cm and 0.49 ± 1.43 cm can be achieved, respectively. Other techniques rely on using kinematic model or constraints conditions based on physiological angle excursions, to improve trajectory estimation. In [33] for example is shown how is possible to reconstruct joint angles and optimizing the estimation by incorporating joint movement physiological limitations and characteristics of the tasks, that in this case was a repetitive writing task. By applying constraints and knowing the bounding box in which the movement was contained, by forcing the the elbow and wrist joint centers to remain within the workspace boundaries the inertial drift error are minimized. The percentage decreases in the root mean square average errors amounted to about 13% in the time intervals when constraints were active.

1.5 Estimating orientation from inertial data

Orientation estimation is necessary, as seen in the previous section, to transform the acceleration data from local reference system into the global reference frame. This is done because, if acceleration was integrated directly in the local frame, errors would accumulate due to change in sensor orientation. For example, if the IMU rotates while recording acceleration, integration in the local frame would incorrectly interpret a change in orientation as a change in position. Also, in the global reference system the direction of gravity along each axis is known and could be easily removed, while trying to remove it in the local system could be problematic and residual bias make error rise during double integration. Once this transformation is achieved, double integration of accelerometer data, after removing the effect of gravity, can be performed and position can be correctly estimated. If a kinematic model with multiple IMUs is used, knowing the orientation of each body segment allows for the reconstruction of the overall body pose.

1.5.1 Sensor fusion approaches

One common technique for estimating orientation is sensor fusion which consist in combining gyroscope, accelerometer and magnetometer data. Sensor fusion approaches are commonly divided in complementary filters and Kalman filter. The first combine the different spectral characteristic of the signal, while accelerometers and magnetometer are more sensible to high frequency noise, and thus give a "low frequency" estimation of the sensor's attitude, the gyroscope is more sensible to drift (low frequency) error and thus give a more "high frequencies" estimation. By combining the different spectrum features it is possible to improve results. Kalman filter, on the other hand, relies on probabilistic modeling, by describing covariance matrix of state and noise to apply non linear correction based on previous estimation of the sensor's position and orientation.

An approach for complementary filter for orientation estimation is proposed by Madgwick [34], the filter employs quaternions to represent orientation. An analytically derived and optimized gradient-descent algorithm is utilized to compute the direction of the gyroscope measurement error by adjusting the sensor measurements with the current quaternion estimate. A gain coefficient β, accounts for the magnitude of correction applied to the quaternion. β can be set based on the expected noise levels in the accelerometer and magnetometer data. If the sensor noise is high, β should be smaller to avoid excessive correction. The estimations are done by integrating over time gyroscope's angular velocity to estimate the change in orientation, then accelerometer dat are used to correct the quaternion by aligning the estimated gravity vector (derived from the quaternion) with the measured gravity vector. The results show an error on roll, pitch and yaw angles comparable or slightly better than Kalman filter method (around 0.7°).

In [22], five sensor fusion algorithms for motion tracking are analyzed, each reconstructing both trajectory (position) and orientation using IMUs, on a singular subject on which several movements that involved one functional degree of freedom at a time, namely elbow flexion/extension, forearm pronation/supination, shoulder flexion/extension, shoulder abduction/adduction and shoulder internal rotation. The first method models a kinematic chain with a Kalman Filter to estimate position and orientation, achieving a 38.8 mm error in simple motions but increasing to 108.9 mm in shoulder flexion. The second method, using quaternion-based estimation and a QUEST algorithm for drift correction, suffers from cumulative errors due to inaccurate acceleration modeling, leading to 89.2 mm and 121.4 mm errors in elbow and shoulder flexion, respectively.

The third method applies a complementary filter to reduce drift, performing well in its "pure" version with a 45.7 mm error in elbow flexion but showing high variability in its "perfect" version, with errors reaching 272.2 mm in shoulder abduction. The fourth method integrates five MIMUs and a camera reference, significantly improving accuracy by counteracting drift, achieving 75.7 mm and 82.7 mm errors in elbow and shoulder flexion. The fifth method, using an Unscented Kalman Filter to better handle nonlinearities, improves dynamic tracking but remains prone to drift, with errors of 89.2 mm in elbow flexion and 214.4 mm in shoulder flexion.

Overall, the error in wrist position reconstruction differ based on task and the method used, the fourth method, combining Extended Kalman Filters with a camera reference, provides the most stable trajectory estimation by minimizing drift during flexion/extension. The first and third methods offer moderate accuracy but struggle in complex movements, while the second and fifth methods accumulate significant drift over time, making them less reliable for long-term tracking.

A review on sensor fusion approaches [35], in which ten different sensor fusion approaches are compared, shows no statistical difference when parameters are properly tuned, in nine different scenarios, with absolute errors ranging between 3.8° and 7.1° for three commercial use sensors.

Trajectory estimation from inertial data presents significant challenges due to sensor noise, drift, and integration errors. The reviewed approaches attempt to mitigate these issues through different sensor fusion techniques and kinematic modeling. Double integration of accelerometer data, although simple, suffers from severe drift unless constraints such as ZUPT or physiological movement limits are applied. Even with such corrections, accuracy depends heavily on the detection of static phases and careful filtering. Overall, the results indicate that no single approach is universally optimal.

1.6 Aim of the thesis

This work aims to estimate trajectory from minimal set-up consisting in a single IMU positioned on the wrist and few anthropometric measurements, during an upper limb rehabilitation task of reach-to-grasp task (R2G), a common clinical exercise, in which the subject is requested to execute a motion in more phases to extend the arm from a starting position, grasp an object, mimics a functional task (drinking simulation) and returns to the starting position. The task emulates a functional task related to ADLs such as drinking from a bottle of water. The reconstruction must be carried out with minimal set-up and measurements, so that it could be used from distance within a protocol, making it suitable for telerehabilitation purposes.

1.6.1 Novelty of the work

The techniques that will be discussed rely on using movement constraints by formulating an optimization problem that starting from an initial estimation of trajectory, reduces errors compared with direct double integration. While other approaches use complicated models which require a more complex setup, such as kinematic chains, with multiple IMUs, or KF and EKF, which require to describe process covariance matrix and noise covariance matrix, the approach used in this work requires minimal setup and measurements, making it an alternative for telerehabilitation applications, for assessing clinical parameters from distance.

1.6.2 Outline

This work is divided as follows:

- This first chapter of introduction on the necessity of telerehabilitation, physical principles of technologies for human motion analysis and methods of trajectory reconstruction.

- The second chapter presents the results of a experimental protocol conducted in controlled condition on a single IMU for assessing the sensor performance in trajectory reconstruction, by validating it against a stereophotogrammetric gold standard.

- The third chapter presents different techniques for trajectory reconstruction, applied on a single IMU data obtained during a R2G protocol, and validated with a stereophotogrammetric gold standard.

- Final conclusions.

For both second and third chapter the same IMU and stereophotogrammetric sensors are used.

Chapter 2

Validation of IMU

2.1 Introduction

As seen in previous sections, trajectory estimation could give objective parameters and help clinicians in asserting effectiveness of rehabilitation and provide important information regarding the clinical situation of a patient. By using IMUs is possible to create telerehabilitation protocols easy to set up, thanks to their high wearability, accessibility and low cost compared with other methods. The chosen inertial sensor for this experimental test was the BlueBuddy (BB) sensor, due to its availability, but before testing its trajectory reconstruction result on a more complex task such as R2G is important to assess performances on simple and more controllable movements, such as uniaxial movement. So, a test bench was built to achieve controlled conditions and ensure the repeatability of the trials to judge the performance of the BB-trajectory reconstruction.

2.2 Materials

2.2.1 BlueBuddy device

The BB is a wearable inertial sensor, represented in fig.2.1, developed at BIOLAB (Politecnico di Torino). It is a nine-axis MIMU (equipped with a triaxial acclerometer, a triaxial gyroscope, and a triaxial magnetometer), it uses LSM9DS1, STMicroelectronics, Geneva, Switzerland; fullscale: ±16 g, ±16G and ±2000 dps. It is provided with Bluetooth Low Energy module, a floating-point microcontroller (SAME70, Microchip, Chandler, Arizona, USA).

Calibration of the device was done prior to the experiment, based on the guidelines provided by Stancin et al. [36]. This calibration process uses a linear response characteristic (2.1),

$$\mathbf{q}_s = \mathbf{K} \cdot \mathbf{V} \cdot \mathbf{q} + \mathbf{q}_0 \tag{2.1}$$

where $\mathbf{q}_s$ is a 3×1 vector representing the measured quantities along each axis, $\mathbf{K}$ represents the 3×3 sensitivity matrix, $\mathbf{V}$ is the 3×3 misalignment matrix, $\mathbf{q}$ is a 3×1 vector with the real values, and $\mathbf{q}_0$ is the 3×1 bias (zero-level offset) vector.

To calibrate the sensor, it is necessary to compute both $\mathbf{q}_0$ and $\mathbf{C}_s$ (the calibration matrix), which is the product of $\mathbf{K}$ and $\mathbf{V}$, as shown in (2.2).

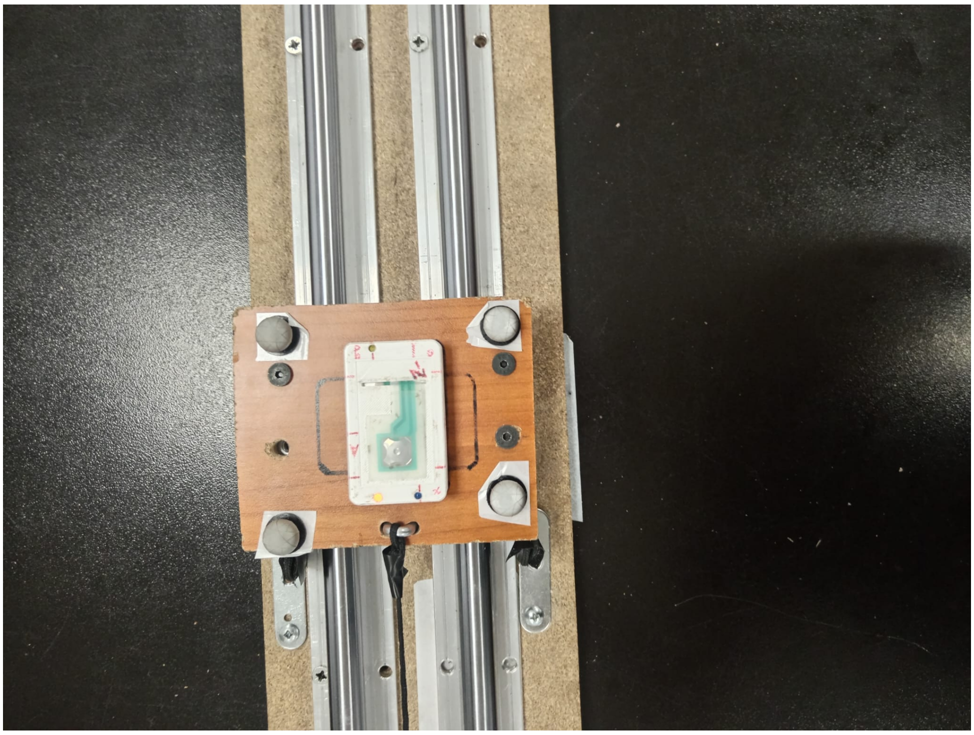

Figure 2.1: BlueBuddy sensor device (BB), mounted on the cart of the workbench before acquisitions.

$$\mathbf{q} = \mathbf{C}_s \cdot (\mathbf{q}_s - \mathbf{q}_0) \tag{2.2}$$

For the accelerometer, the bias vector can be estimated by acquiring static data for an extended period along each axis and in both directions. The mean values for the positive and negative orientations are computed, forming two 3×3 matrices, $\mathbf{A}_{s+}$ and $\mathbf{A}_{s-}$. The bias vector is then calculated as shown in (2.3), where $\mathbf{i}$ is a column vector of ones.

$$\mathbf{a}_0 = \frac{(\mathbf{A}_{s+} + \mathbf{A}_{s-}) \cdot \mathbf{i}}{6} \tag{2.3}$$

Averaging multiple samples reduces the noise by a factor proportional to the number of captured samples.

Gyroscope calibration requires a static acquisition in an arbitrary position, followed by three separate acquisitions where the sensor is rotated along each axis at a known angular velocity, or subjected to a constant angular velocity for a fixed duration. The total angle is then computed as the integral of angular velocity over time and compared to the theoretical value.

Using (2.4), where $\mathbf{\Omega}_o$ is the 3×3 matrix containing the mean static acquisition along each axis, and $\mathbf{\Omega}_s$ is the 3×3 matrix of the sensed angular velocities, we obtain (2.5). Here, $\mathbf{\Omega}$ represents the theoretical angular velocity that would be measured by an ideal gyroscope.

$$\mathbf{\Omega}_s = \mathbf{C}_s \cdot \mathbf{\Omega} - \mathbf{\Omega}_o \tag{2.4}$$

$$\mathbf{C}_s = (\mathbf{\Omega}_s + \mathbf{\Omega}_o) \cdot \mathbf{\Omega}^{-1} \tag{2.5}$$

By computing the calibration matrices and bias vectors, more precise measurements can be obtained. In fig. 2.2, both the Vicon and BB reference systems are displayed. The BB sensor orientation was adjusted by a 90-degree rotation around z axis after each trial, following the guide drawn on the cart.

2.2.2 Vicon system description and setup

A stereophotogrammetric system was employed as gold standard for the tracing of the trajectory (Vicon T20, Vicon Motion Systems, Yarnton, Oxfordshire; sampling frequency: 100 Hz). The analysis was recorded in the Motion Analysis Laboratory of PolitoBIOMed Lab in Politecnico di Torino. The system uses twelve infrared cameras to reconstruct positions of markers in the scene; four photo-reflective markers (diameter: 9.5 mm) were attached around the BB on the cart, so that a local reference system with axis parallel to BB reference system could be defined. Vicon system was calibrated as well; first by having it warmed up for around one hour and then, following the calibration process provided by Vicon instructions [37]. These consist in first obscure any reflective noise caused by other light sources, then the provided calibration wand is used to correctly calculate the intrinsic and extrinsic parameters of the cameras. This has been realized by waving the wand in front of each camera so that a sufficient number of samples were collected by each camera. The wand in fact has reflective markers in known position relative to each other. A Vicon reference system has been chosen, whose origin does not need to be coincident with the reference system used by BB, they differ only in a translational movement plus a rotation to have the axis coincident. To compute slide distance is sufficient to calculate the difference between initial position at the start of the slide and final position at the end of the slide. In fig. 2.2 both Vicon and BB reference systems are displaed, they have parallel axis but different verses.

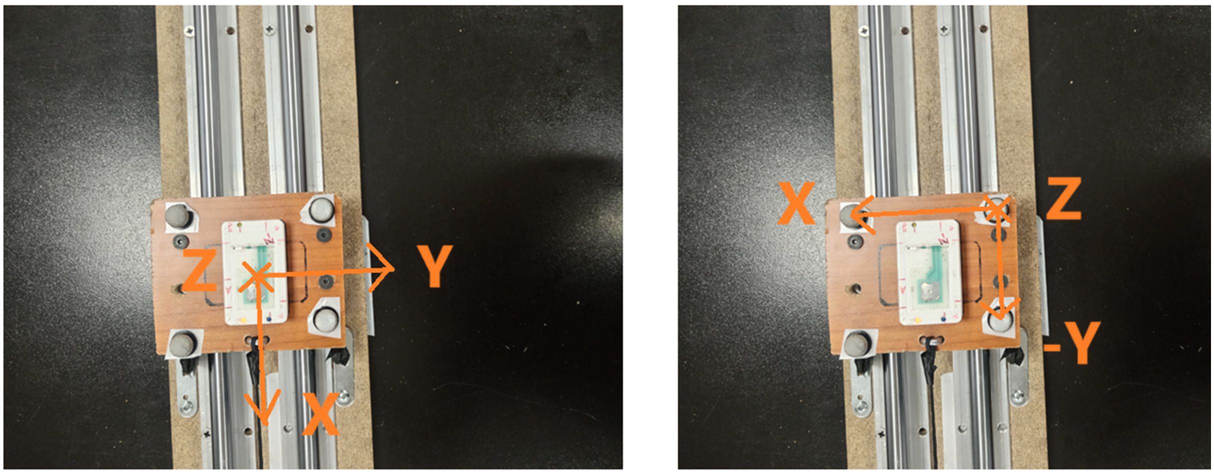

Figure 2.2: On the left is the BB reference system, and on the right is the Vicon reference system. During the trial, the BB system's x-axis is oriented in the opposite direction of the slide (-x trial) and rotates by 90 degrees from one trial to the next. In contrast, the Vicon system remains consistent across all trials.

2.2.3 Experimental workbench build

To ensure controlled conditions, an experimental workbench was constructed. It features two parallel rails that constrain movement to a single direction, minimizing deviations in the perpendicular axis. A wooden sliding cart, mounted on ball bearings, moves along these rails, allowing precise sensor positioning while reducing friction for smooth motion. The rails are securely fastened to a composite wood base with screws.

The cart is made from precisely cut wood and includes a top-mounted guide to maintain proper alignment of the ball bearings with the rail's direction. Four reference points are designated for accurate placement of reflective markers, establishing the Vicon local reference system.

A pulley system, connected to the cart via a string and counterweight, drives the motion. When the counterweight is released, gravity pulls the cart along the rails. The ball bearings are firmly attached to the cart using wood screws, as seen in fig. 2.4.

When the weight is allowed to fall, by attaching a counterweight to the cart, the cart is moved with constant acceleration, reaching the end of the rail. For this specific experience, a weight of 300 g was chosen and connected by a knot to the pulley.

Finally, the device is equipped with end-course stoppers, which control the sliding distance. These stoppers, located halfway (30 cm) and at the end of the course (60 cm), can be adjusted and are made with L-shaped stirrups fixed to the base with screws.

The device is shown in fig. 2.3.

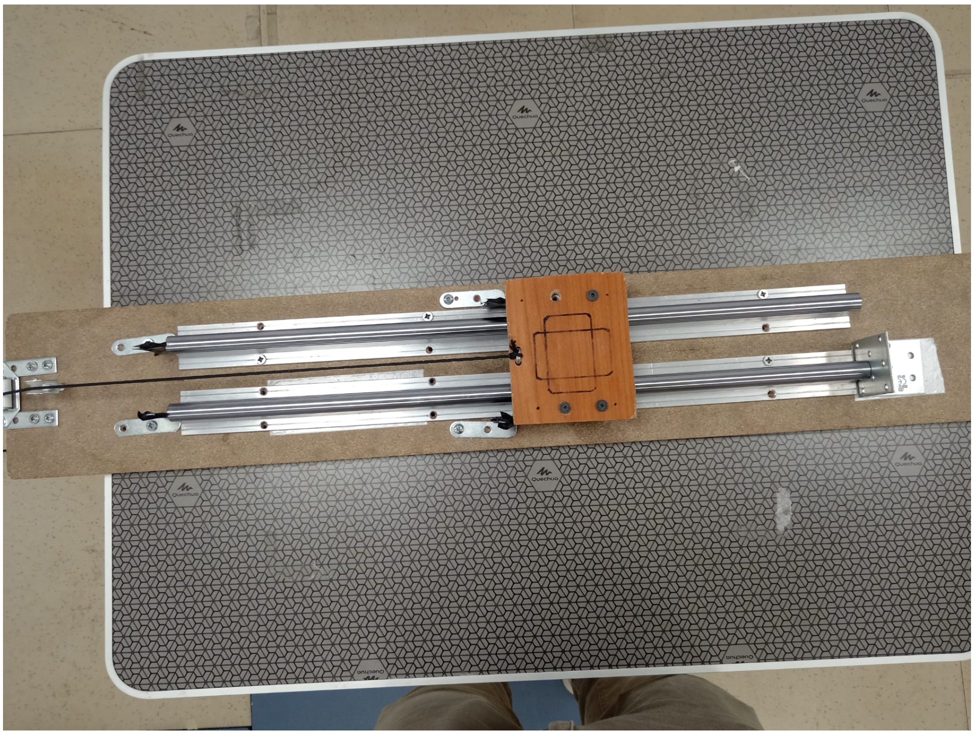

Figure 2.3: Top down view of the workbench; it consists of a double rail with a wooden cart mounted on top and a pulley system to move the cart.

Figure 2.4: Detail of the workbench pulley system.

2.2.4 Experimental protocol

The setup table was bound to the experimental table to limit vibrations effect by using double-sided tape, a constant mass of around 300 g was used as counterweight for the cart to move fig. 2.5 and fig. 2.6. The slide distance was settled to 30 cm, by using stoppers that would arrest the slide, the actual distance covered by the sensor was around 15 cm. The BB was placed on to the cart by using double-sided tape, following a drawn guide to ensure that the direction of the sensible axis was parallel to the rail direction. Reflective markers (9.5 cm diameter) were also put on the cart, to ensure that trajectory could be reconstructed with Vicon. The acquisition protocol consisted in acquiring for two axes (x and y of the BB) in both positive and negative directions a series of 30 controlled slides. For each trial a 1-minute static period was observed, then the device was waved around the sensible axis, to later align the Vicon and BB signals, then another 1-minute static period and then the movement phase started. The cart at the end of the course was manually positioned at the start of it by holding it against the stopper, then after about 10 seconds the grip was released and the cart moved to its starting position thanks to the force applied by the counterweight, finally a 10 seconds static period was observed; this slide process was iterated for 30 times, in order to have a sufficient number of trials and make statistical considerations.

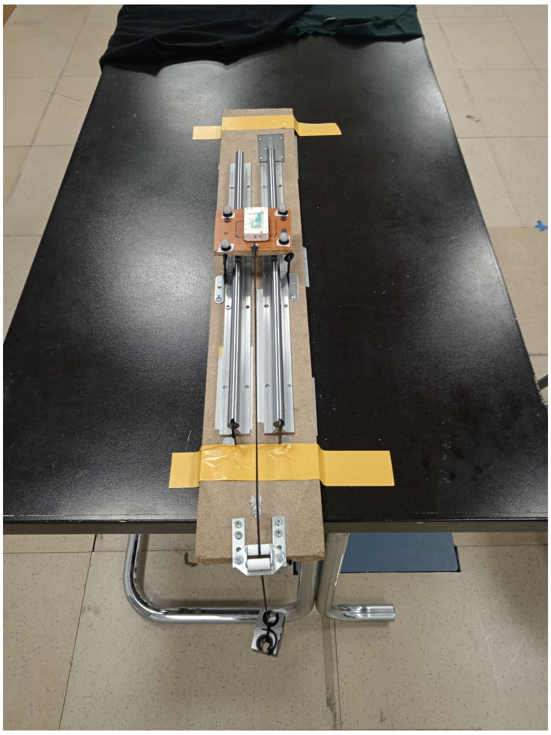

Figure 2.5: Top down view of the workbench set up in the lab constrained with adhesive tape.

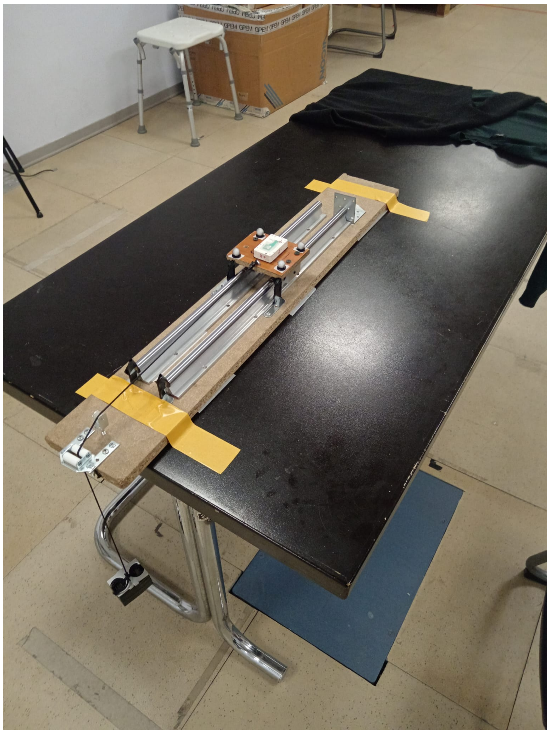

Figure 2.6: Lateral view of the workbench set up in the lab constrained with adhesive tape.

2.3 Methods

MATLAB r2023b software (MathWorks Inc., Natick, MA, USA), was used for analyzing and processing the signals recorded with this protocol. After loading them into the workspace, the first processing was done by resampling and alignment of the signals. A schematic flowchart of the methods is presented in fig. 2.25.

2.3.1 Resampling and alignment of signals

Vicon recording was started right after the start of the recording by BB. The choice of which sample frequency to use for resampling was done by considering that resampling from a lower to higher sample frequency would cause some samples to be found by inaccurate interpolation, so it was decided to resample BB signal (from 115 Hz sample frequency) to Vicon sample frequency (100 Hz). The inertial data was downsampled to a sampling frequency of 100 Hz by using the "interp1" function of MATLAB.

The signals need to be aligned so that is possible to confront the trajectory reconstruction of the gold standard with MIMU based approach. It was used a method based on maximizing the cross-correlation function between the first two minutes portion of the angular velocities signals. In fact, the first two minutes are, by default of the protocol, static acquisition plus a wave movement around the sliding axis. During the wave movement an oscillating pattern emerges in the MIMU signals that will be used as reference for aligning it to Vicon. By using the method proposed by Chardones [38], which describes how to align local frames of inertial and other motion capture system, it is possible to obtain the angular velocities from the global frame (IJK) of Vicon to local frame of reflective markers (ijk) which are aligned with BB reference system. This is achieved by using the information about the difference in rotation matrix in local and global frames at consecutive instants, calculated by using the four reflective markers "O","X","Y" and "A". The rotation matrix (R_{IJK}^{ijk}) is the 3x3 matrix calculated for each time sample by having as the first row the x-axis calculated as the difference in positions between "X" and "O", then normalized to have norm equal to one. A support vector is calculated with similar method by the difference of "Y" and "O", and used to calculate z-axis as the cross product of x-axis and support vector, this is done for making sure of having reference system with axis perpendicular to each other, instead of directly using the difference of "Y" and "O" as y-axis. Then finally the third row is calculated as cross cross product of x and z axis. The variation in orientation in global frame(ΔR^{IJK}) is calculated as the difference at consecutive time samples of rotation matrix (2.6), from which variation in orientation in local frame is obtainable by (2.7). Finally through (2.8),(2.9),(2.10) angular velocities in local frame is calculated.

$$\Delta R^{IJK} = \left(R_{IJK}^{ijk}(t)\right)^{-1} \cdot \left(R_{IJK}^{ijk}(t+\Delta t)\right) \tag{2.6}$$

$$\Delta R^{ijk} = R_{IJK}^{ijk}(t) \cdot \Delta R^{IJK}(t) \cdot \left(R_{IJK}^{ijk}(t)\right)^{-1} \tag{2.7}$$

$$C^{ijk}(t) = \frac{\left|\Delta R_{23}^{ijk}(t) - \Delta R_{32}^{ijk}(t),\, \Delta R_{31}^{ijk}(t) - \Delta R_{13}^{ijk}(t),\, \Delta R_{12}^{ijk}(t) - \Delta R_{21}^{ijk}(t)\right|}{\sqrt{\left(\Delta R_{23}^{ijk}(t) - \Delta R_{32}^{ijk}(t)\right)^2 + \left(\Delta R_{31}^{ijk}(t) - \Delta R_{13}^{ijk}(t)\right)^2 + \left(\Delta R_{12}^{ijk}(t) - \Delta R_{21}^{ijk}(t)\right)^2}} \tag{2.8}$$

$$|\omega^{ijk}(t)| = \cos^{-1}\left(\frac{\Delta R_{11}^{ijk}(t) + \Delta R_{22}^{ijk}(t) + \Delta R_{33}^{ijk}(t) - 1}{2}\right) \cdot \Delta t^{-1} \tag{2.9}$$

$$\omega(t) = |\omega^{ijk}(t)| \cdot C^{ijk}(t) \tag{2.10}$$

As suggested by Bergamini et al. [39], to obtain more reliable angular velocity estimation from stereophotogrammetric recording, is necessary to first filter the trajectory acquisitions and improve the quality of signal by removing high frequencies noise, in this case a 6 Hz second order low pass Butterworth filter was used.

Then is computed the cross-correlation function between BB norm of angular velocity from gyroscope data, and norm of angular velocity from Vicon data using Chardonnens method, using only the first two minutes of the signals. In fig. 2.7 are shown the results before and after alignment for the norm of angular velocity. in fig. 2.8, a magnification, displaying the movement used to align the two signals.

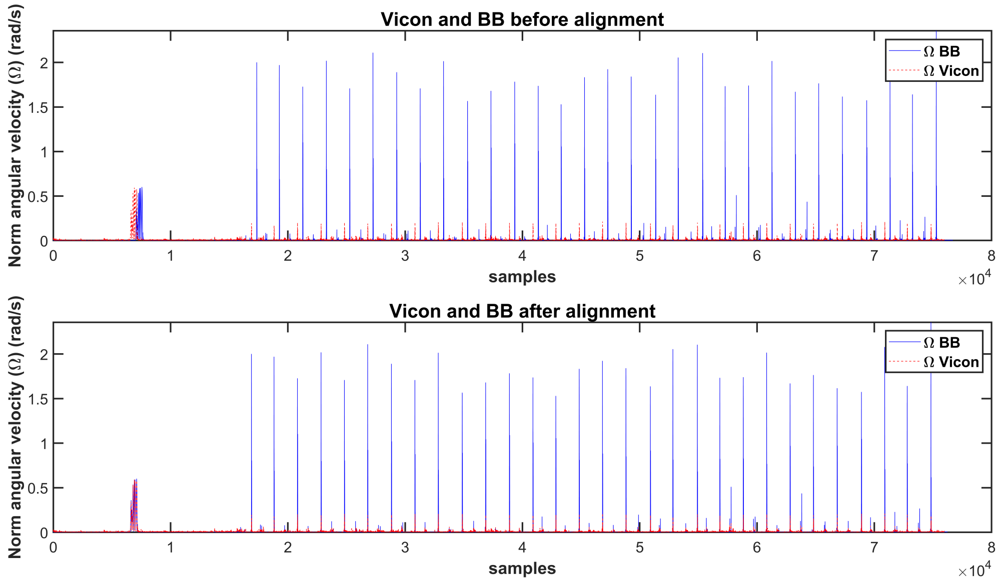

Figure 2.7: Norm of angular velocities calculated with Chardonnes method from Vicon data (red) and from BB after mean removal (blue), before and after alignment.

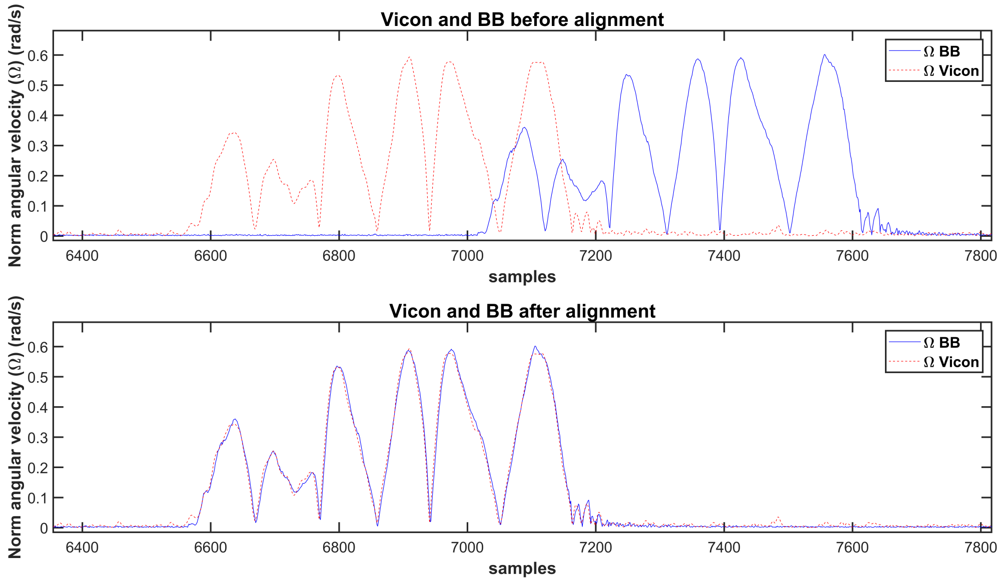

Figure 2.8: Magnification of the first two minutes of 2.7. The delay is calculated over this portion, by maximizing cross correlation of the two signals.

2.3.2 Gravity removal

To compute the trajectory is sufficient to calculate the displacement in every direction at each time sample, double integration of acceleration is the simplest method; however, the accelerometer records also gravity vector. So, it is necessary to first remove the mean value over a static acquisition, otherwise drift errors will occur. Raw acceleration and angular velocities data recorded by BB for the acquisition are shown in fig. 2.9. In fig. 2.10 a magnification.

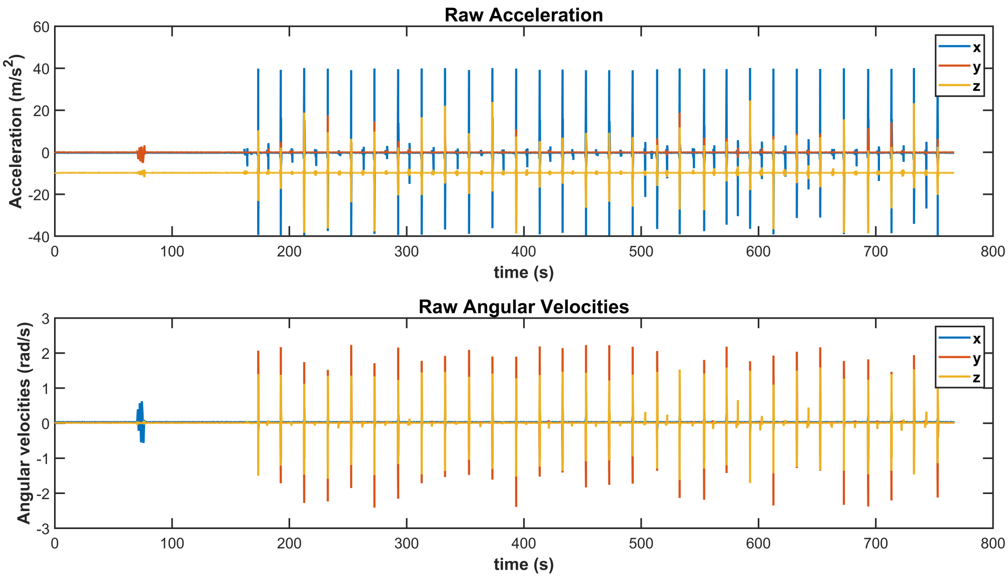

Figure 2.9: Raw acceleration and angular velocity signals obtained directly from BB.

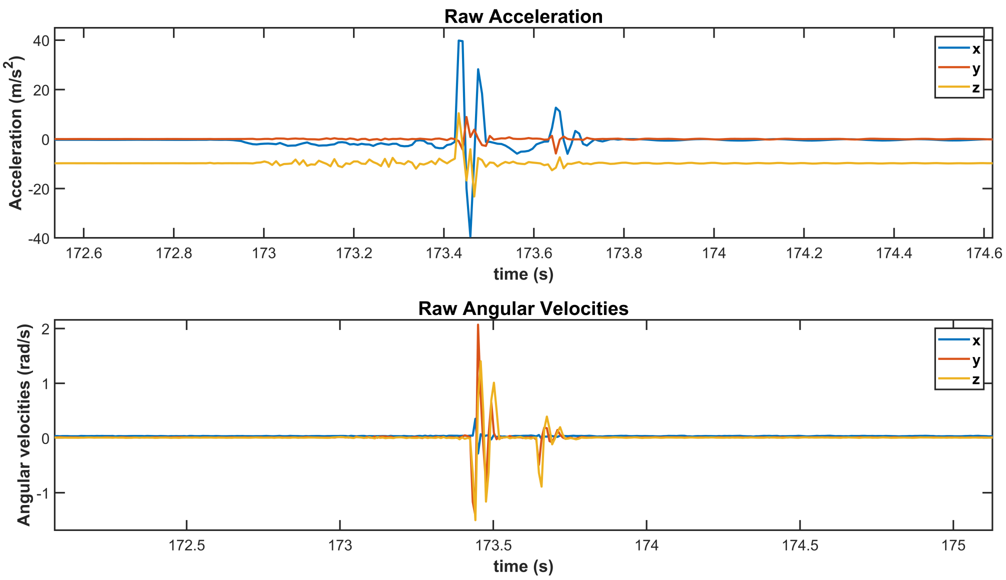

Figure 2.10: Magnification of 2.10, over a singular slide movement.

The static period is considered as the first minute of static acquisition; acceleration and angular velocities data after mean removal are shown in fig. 2.11. In fig. 2.12 a magnification.

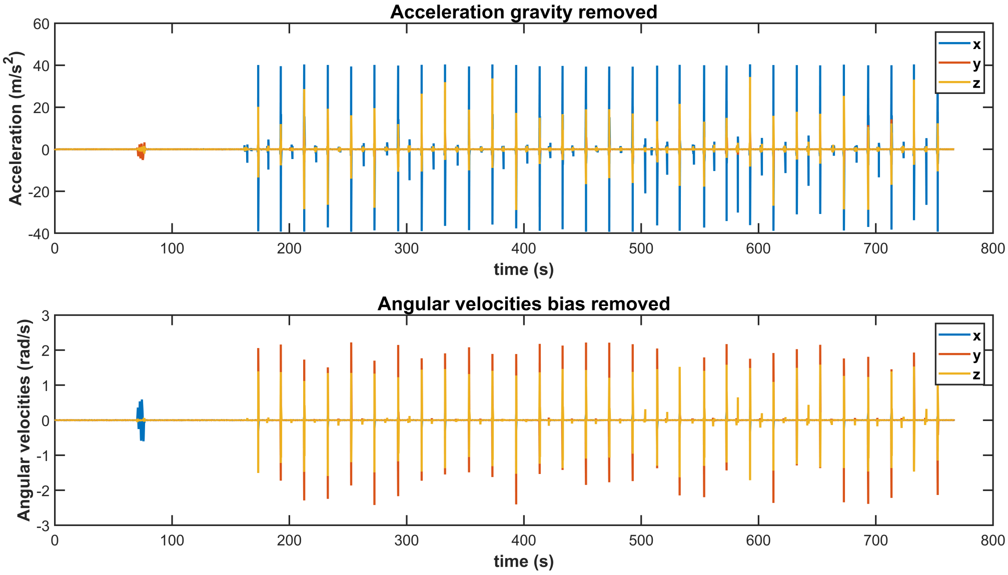

Figure 2.11: Acceleration and angular velocity signals obtained directly from BB after mean removal.

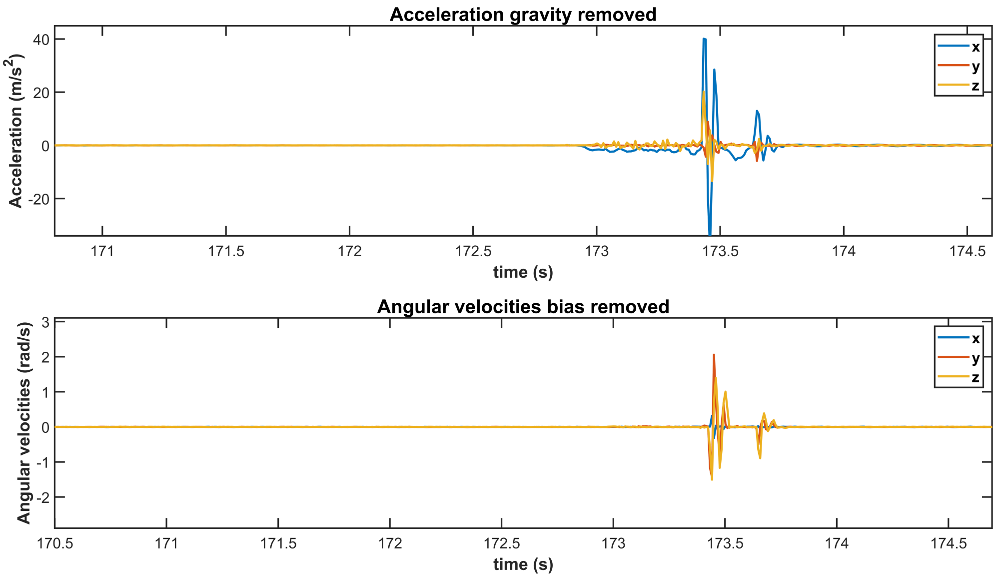

Figure 2.12: Magnification of 2.11, over a singular slide movement.

It is possible to divide each slide movement in three different phases, a first phase in which a manual movement moves the cart at the start of the course, the second phase, after few seconds from the first, in which the cart is subjected to acceleration by the counterweight mass and immediately after, the third phase, a dynamic collision at the end of the course in fig. 2.13.

The third phase, with higher accelerations must not be considered in the integration process because it does not belong to the slide movement but it is caused by the collision; also the first phase is not significant for the validation of the device, so only the middle phase must be considered for double integration. To do that, for each slide it was found the position of the time sample corresponding to the collision, and considered a portion of the signal one second before and after the peak, corresponding to the second and third phase. A signal with only the third and second phase was generated by concatenating each slide as shown in fig. 2.14.

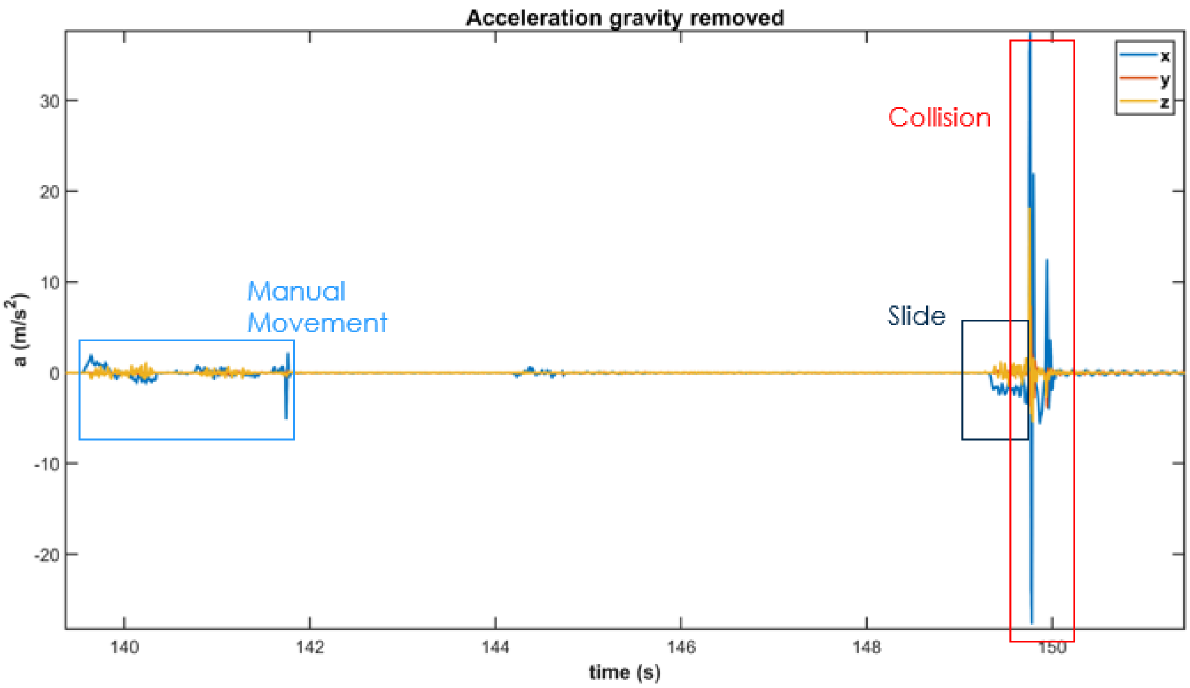

Figure 2.13: Example of the acceleration signal during a single trial of the protocol; in the first part the cart is moved to the start of the course (blue box), then after a static period is released with a constant step acceleration (black box). Right after an high acceleration spike from collision (red box), followed by another period of static before the repetition of the process.

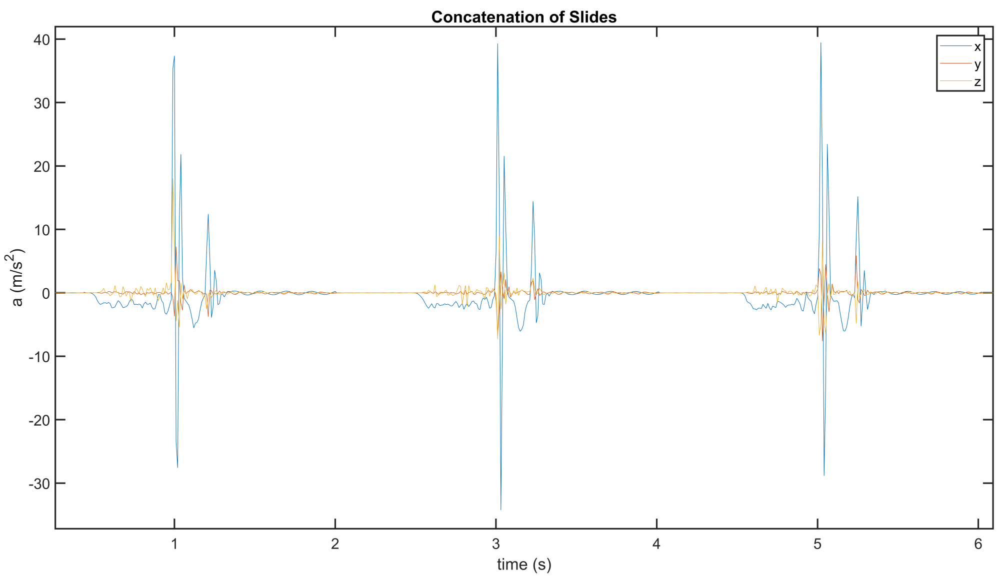

Figure 2.14: Each acceleration slides movement are concatenated in a single signal

2.3.3 Template matching

To extract the second phase only, relative to the slide movement, it is used a method based on template matching; using the portion of signal calculated in the previous step, and averaging them, a template signal is calculated. As expected, the averaging result has a constant step-acceleration for the slide phase, and a sinusoidal exponentially damped acceleration for the collision phase. In fig. 2.15 through fig. 2.18, are shown for each trial along each different axis, the four templates obtained by averaging the acceleration concatenated signals, with BB positioned with its axis coincident to the direction of the slide, along with the manually chosen starting and ending points for integration.

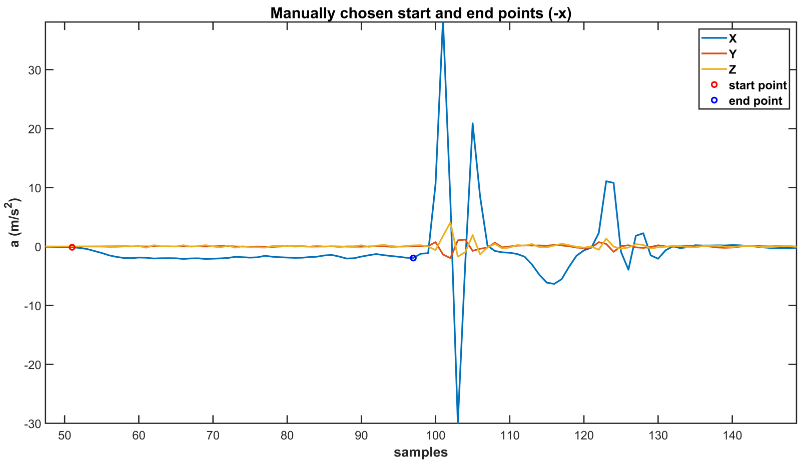

Figure 2.15: Slide template obtained by averaging, with BB -x axis coincident with the direction of the slide.

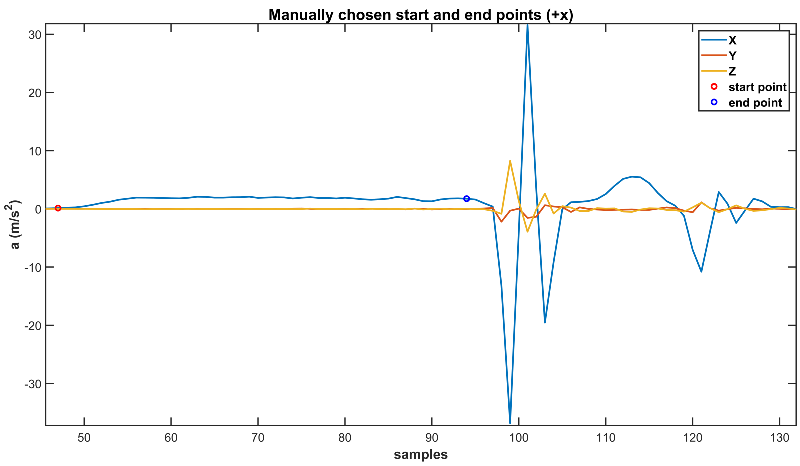

Figure 2.16: Slide template obtained by averaging, with BB +x axis coincident with the direction of the slide.

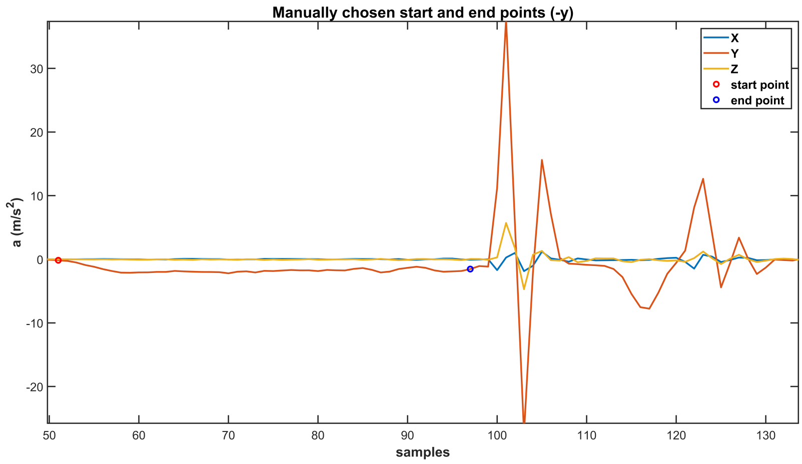

Figure 2.17: Slide template obtained by averaging, with BB -y axis coincident with the direction of the slide.

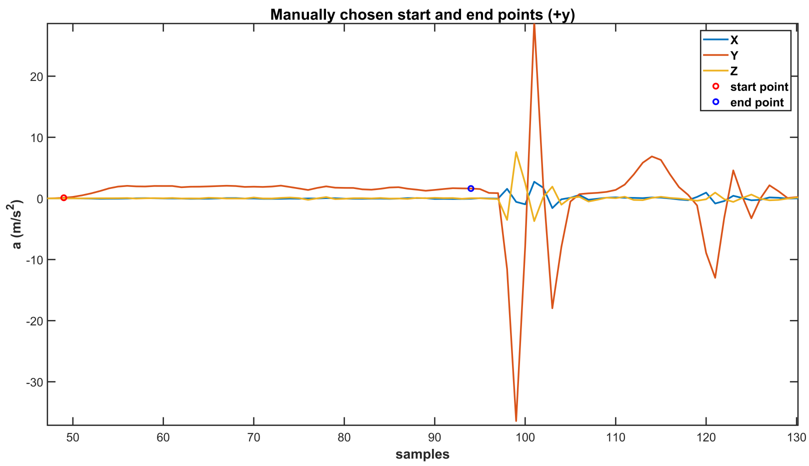

Figure 2.18: Slide template obtained by averaging, with BB +y axis coincident with the direction of the slide.

Now, by calculating the cross-correlation between the template norm and the original signal norm, thirty local maximums emerge, corresponding to the time sample that best fit the template. By choosing reasonable points for the start and end of the slide on the template is possible to map them on each corresponding start and end of the slide movement over the original signal.

In fig. 2.19 (magnified in fig 2.20), as representative example is shown for each trial along each different axis, the mapping of the points by using this template matching method for slide along -x axis.

Having now the starting and ending point of the slide and having removed the mean value over the static acquisition, by simply integrating over time for two times, the acceleration signal over each corresponding duration, an estimation of trajectory is obtained for each movement. To extract instead the trajectory, from raw Vicon data in fig. 2.21, (magnified in 2.22), is sufficient to calculate the difference in position between the start

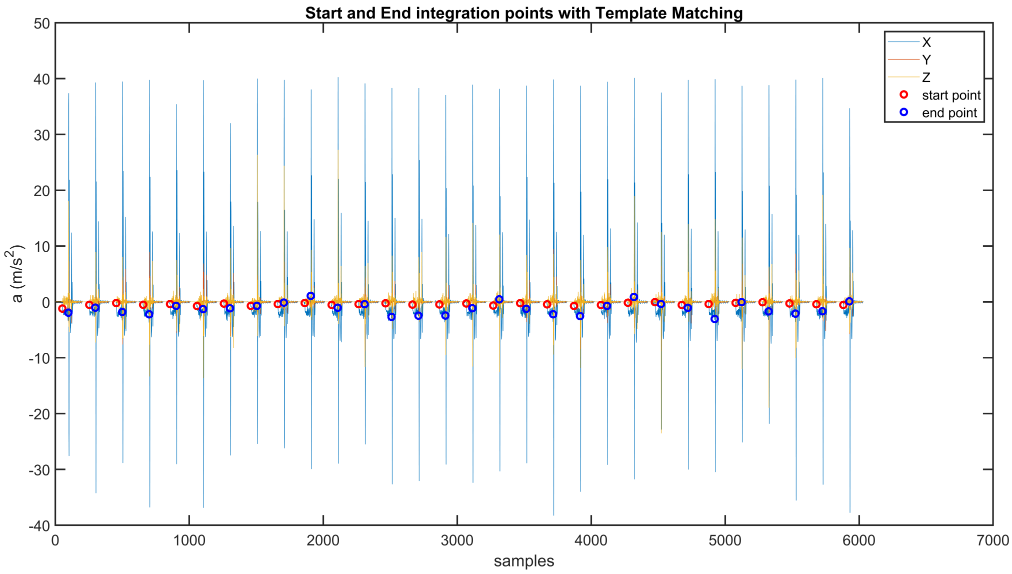

Figure 2.19: Starting and ending points found on concatenated signal with template matching method (-x).

and end of the slide, individuated by using the same time samples calculated with the template matching method, as seen in fig. 2.23 (magnified in fig. 2.24). Then to better visualize the results, the norm of trajectory is calculated for both Vicon and BB and converted to the same reference system.

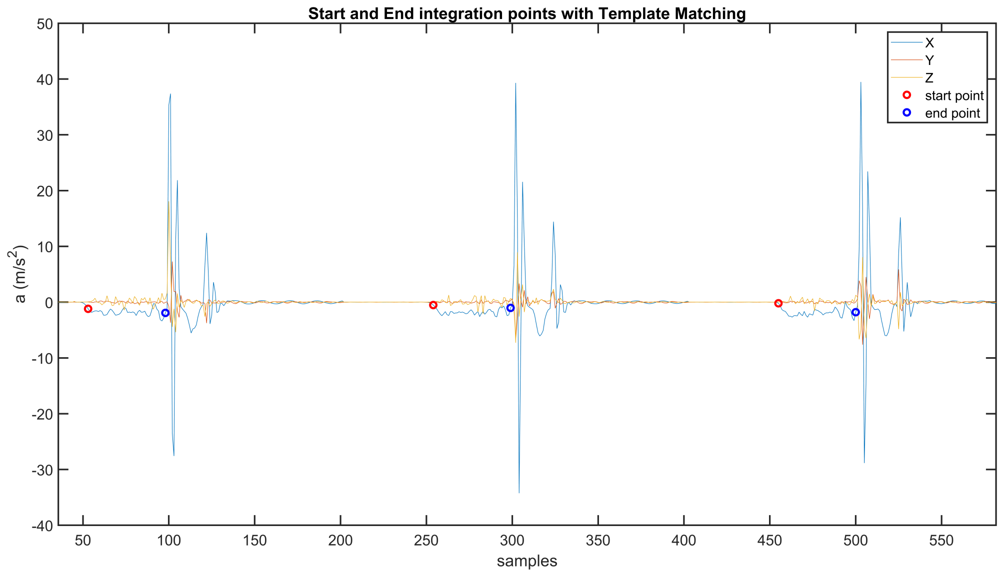

Figure 2.20: Magnification of 2.19.

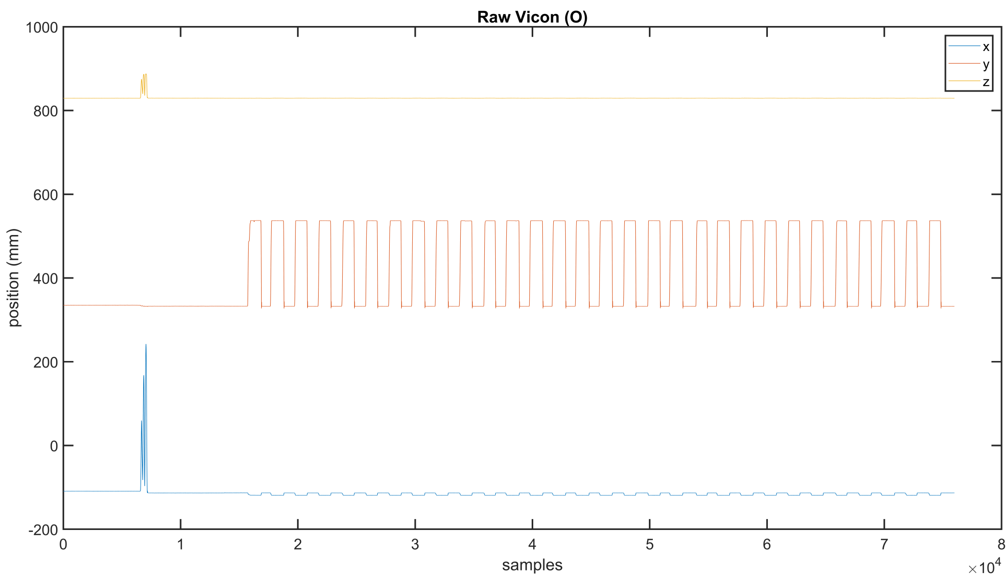

Figure 2.21: Vicon raw position signal from marker ”O”.

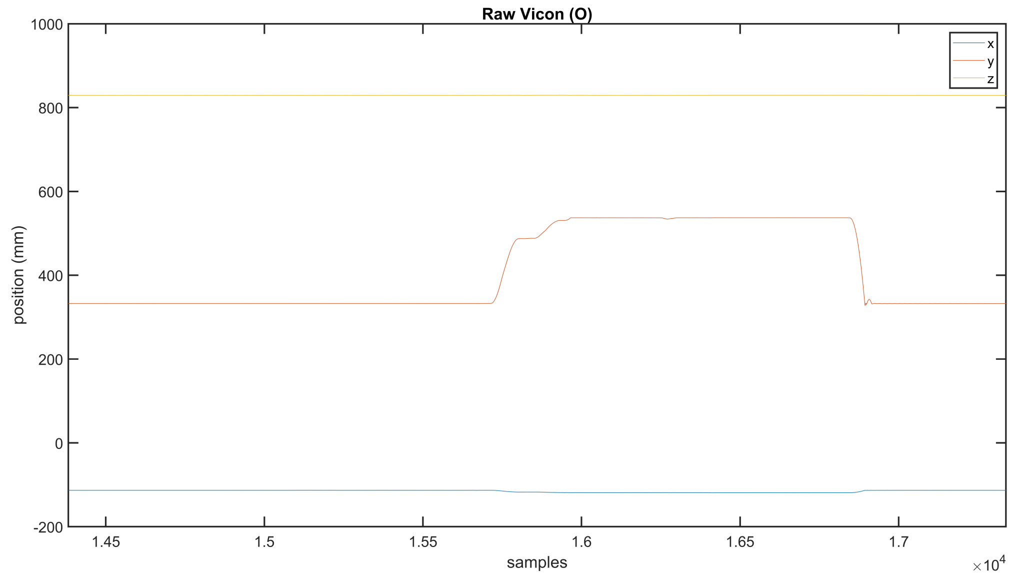

Figure 2.22: Magnification of 2.21.

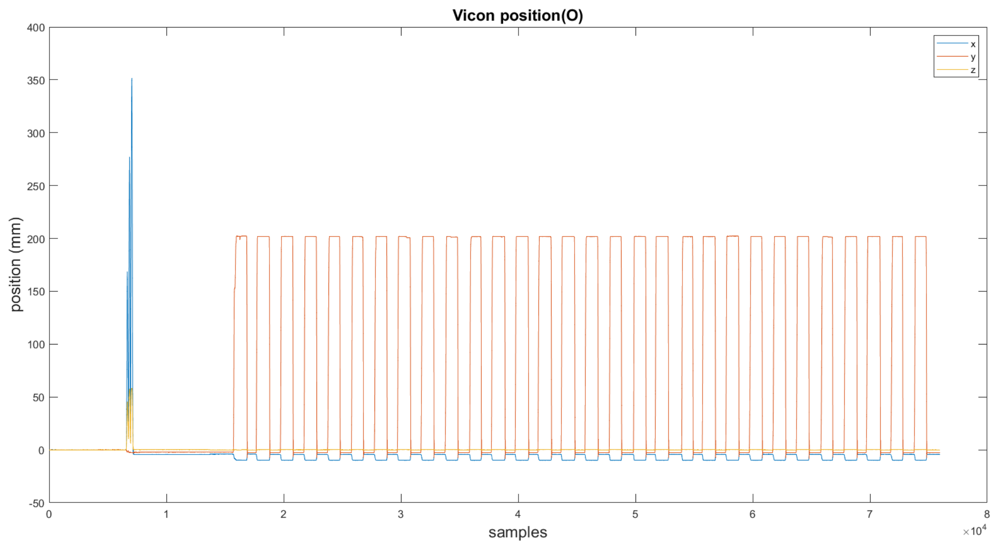

Figure 2.23: Vicon position signal from marker "O" after mean removal

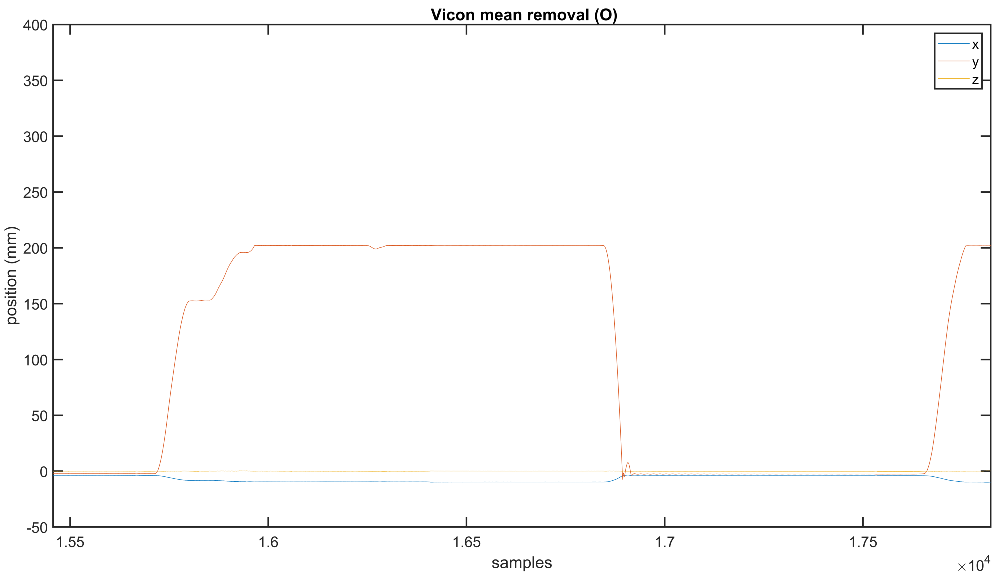

Figure 2.24: Magnification of 2.23.

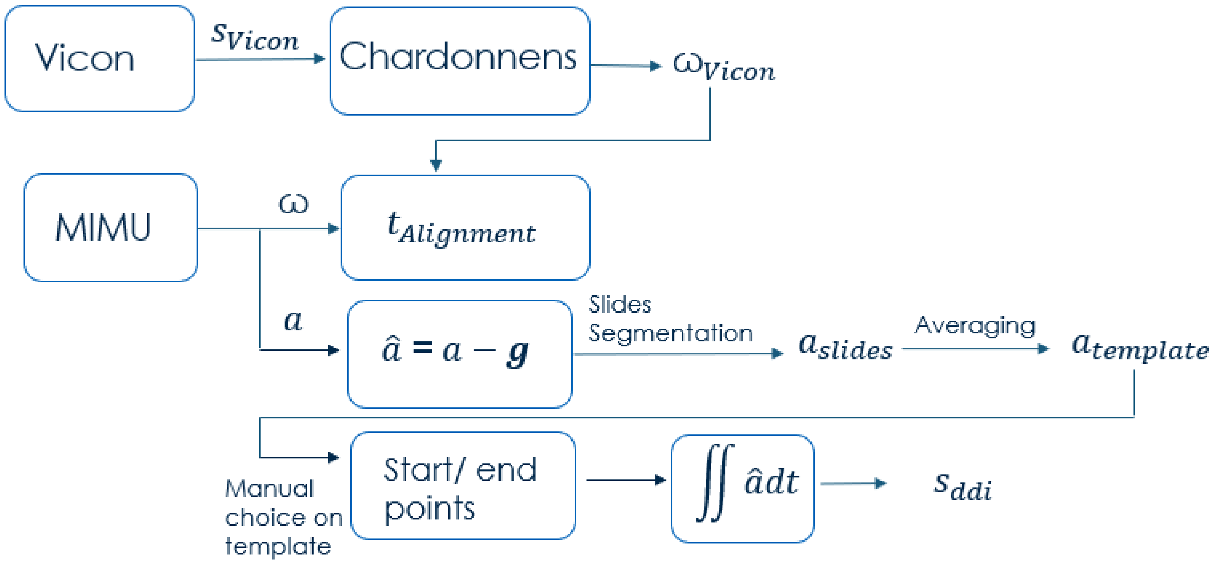

Figure 2.25: Flowchart of the first experience. It is first used displacement from Vicon system to calculate angular velocity using Chardonnens method [38]. The two system are aligned by calculating delay among their angular velocities in the first 2 minutes. Gravity is removed from acceleration retrieved by the IMU and portion relative to the slides are found through a segmentation algorithm. By averaging each slide trial a template is generated and by manually choosing slide starting and ending points on the template, starting and ending points are found over all the trials. Finally, a double integration of acceleration is computed between each couple of start and end point.

2.3.4 Statistical Analysis

After trajectory estimation for each trial, a statistical analysis was conducted on final displacement estimation. It was applied a Lilliefors test to assess the data distribution normality on norm of final displacement (significance level α equals to 0.05).

It was verified that both Vicon and BB data followed a normal distribution by rejecting the null hypothesis (H=0). Then a paired Student t-test has been carried on between gold standard and the experimental method to see if a statistical difference of the mean value of the final displacement norm could be observed. The tests were done by using a significance α equals to 0.05 (two tails), using MATLAB built in functions "ttest" function.

2.4 Results

In table 2.1 are reported the absolute error for norm trajectory of final displacement for each axis tested.

2.4.1 Trajectories

Results of estimated norm trajectories using double integration of inertial data are shown in fig. 2.26 through fig. 2.29, along with Vicon reference; in lighter shade is represented the range of the two methods, in dashed line the mean norm trajectories.

Table 2.1: Final displacement errors

	mean ± std (cm)	mean ± std (% of ROM)
X+	1.17±0.92	6.8±4.2
X-	1.22±0.84	6.4±3.9
Y+	1.24±0.81	6.9±4.2
Y-	1.01±0.63	6.4±4.3

In the table, the mean absolute errors for final displacement and errors on final displacement as percentage of ROM measured on Vicon are shown. The results are presented as mean value ± standard deviation for each axis tested. std: standard deviation.

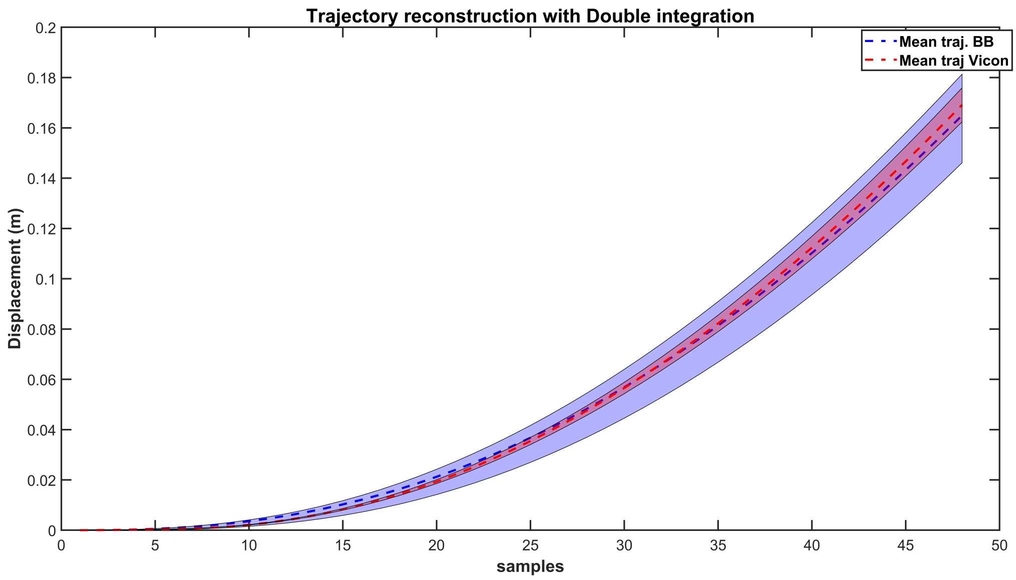

Figure 2.26: Norm trajectory reconstruction over all trials, in dashed line mean of all trajectories, in light colors range over all trials. In red Vicon gold standard, in blue trajectory reconstructed with BB data by double integration. (-x)

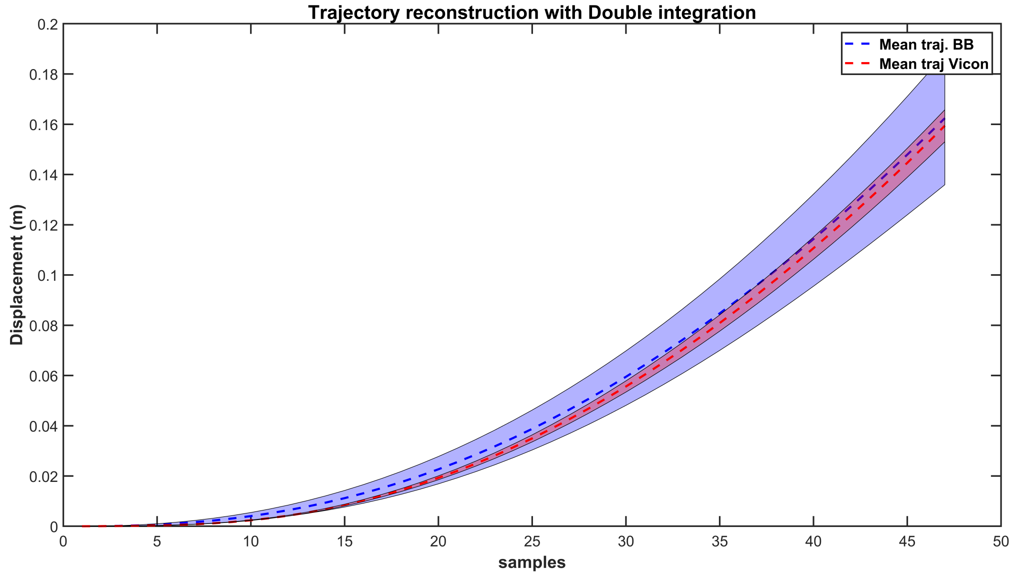

Figure 2.27: Norm trajectory reconstruction over all trials, in dashed line mean of all trajectories, in light colors range over all trials. In red Vicon gold standard, in blue trajectory reconstructed with BB data by double integration. (+x).

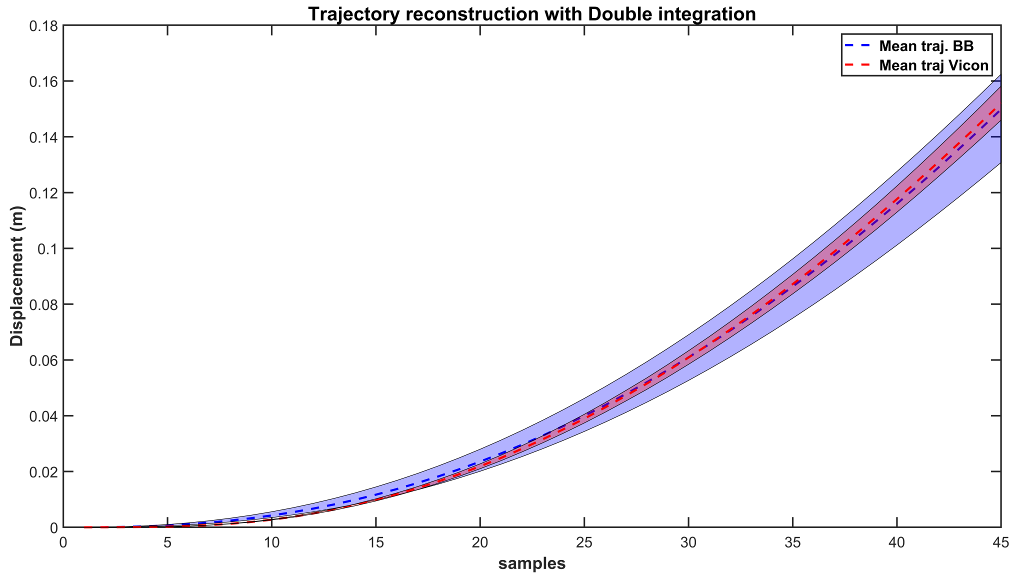

Figure 2.28: Norm trajectory reconstruction over all trials, in dashed line mean of all trajectories, in light colors range over all trials. In red Vicon gold standard, in blue trajectory reconstructed with BB data by double integration. (-y).

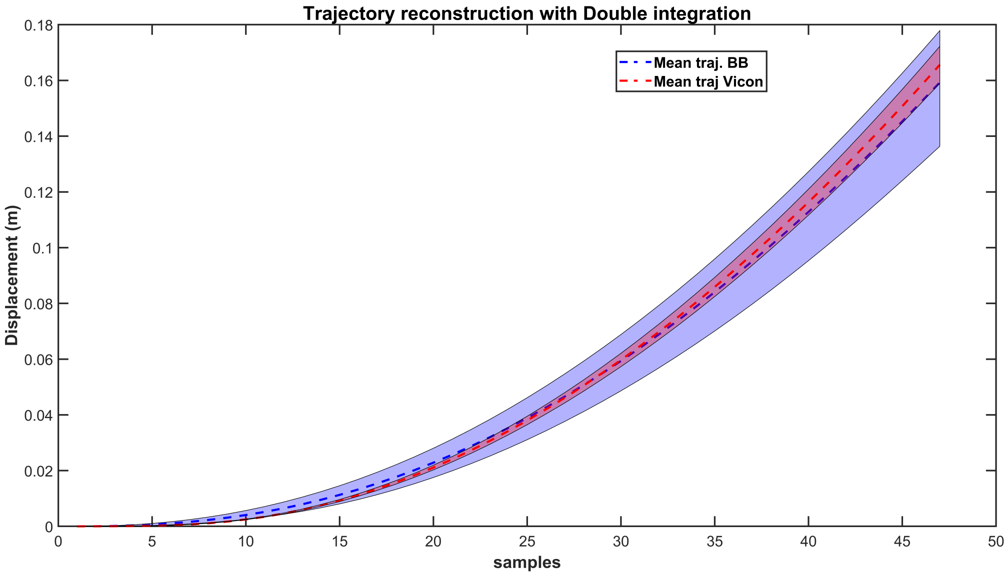

Figure 2.29: Norm trajectory reconstruction over all trials, in dashed line mean of all trajectories, in light colors range over all trials. In red Vicon gold standard, in blue trajectory reconstructed with BB data by double integration. (+y).

2.4.2 Statistical Analysis

In fig. 2.30, are presented paired student test results norm of final displacement, with mean ± standard deviation along with p-values results. Every t-test done show to not refuse the null hypothesis (H=0), with p-value for every test higher than significance level, i.e. there is no statistical difference between the two methods (x-; p=0.092, x+; p=0.213, y-; p=0.160, y+; p=0.202).

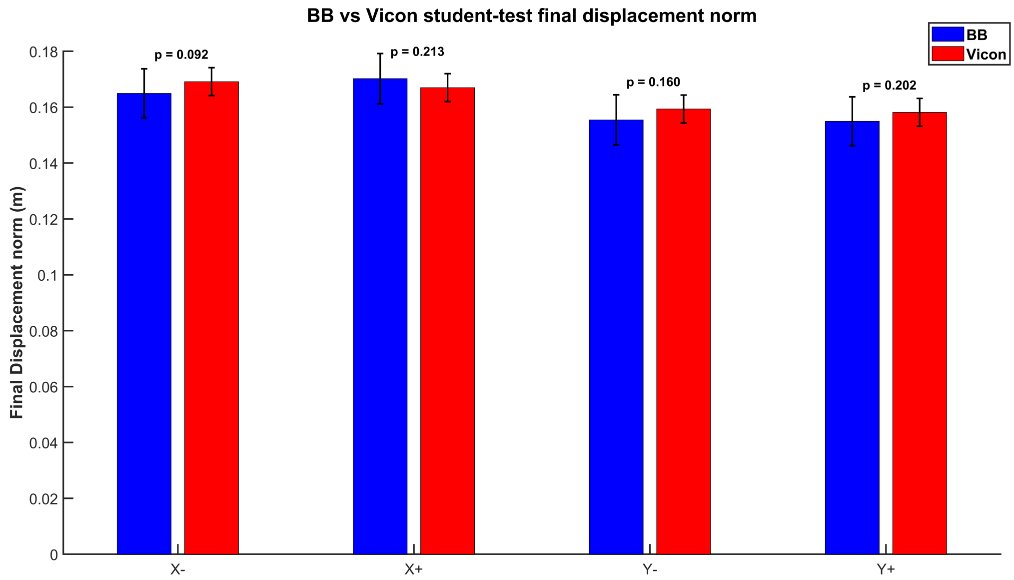

Figure 2.30: ttest results over final norm displacement, for each trial (-x,+x,-y,+y). No asterisks means no significant difference between the two methods (p value>0.05)

2.4.3 Errors

In fig. 2.31 through fig. 2.34 are shown the absolute errors over time for norm trajectory estimation over each trial, in lighter color the i-th slide and in dashed dark color the mean error over time; the error tends to increase over time as expected due to cumulation of integration error. Errors distributions on final displacement are also calculated as the mean of the final displacement of the norm trajectories, both as absolute values in fig. 2.35, and normalized by dividing for the norm of Vicon movement fig. 2.36. The mean absolute error in final displacement for every trial is 1±0.7 cm, which correspond to an error of 6±4% of the expected value.

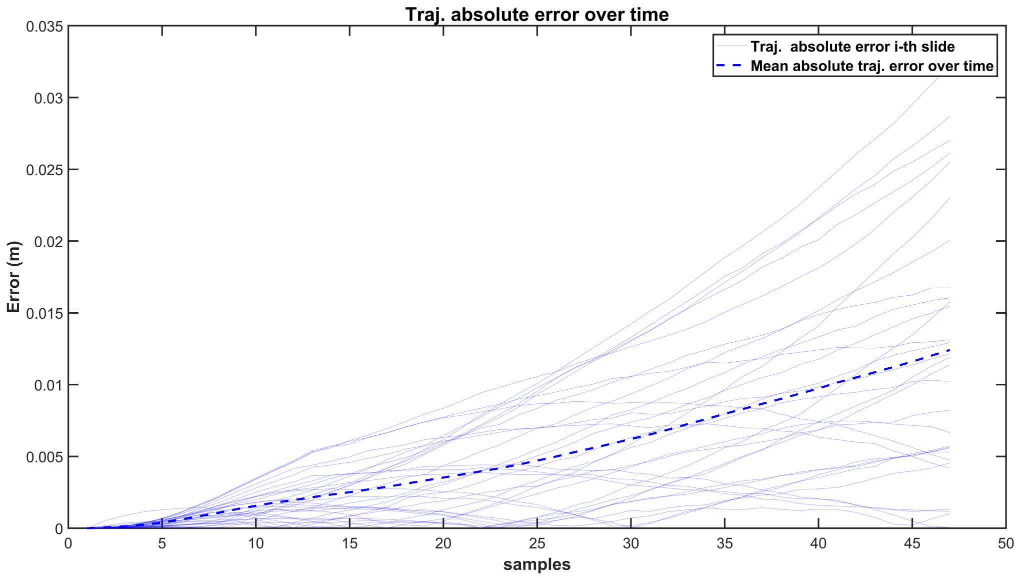

Figure 2.31: Absolute error over time between trajectory norm of Vicon and BB, in light color the singular trials, in dashed line the mean value. (-x).

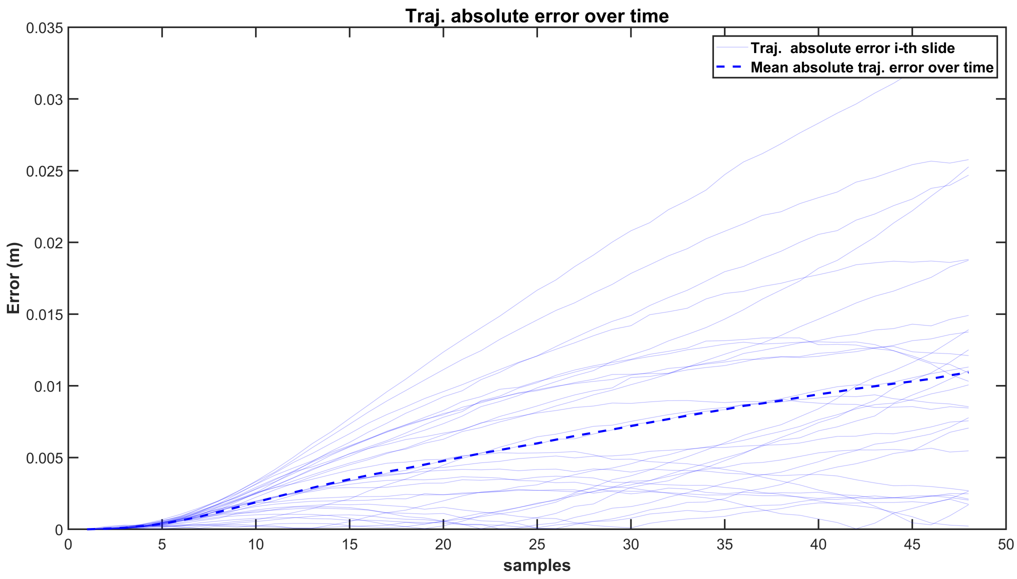

Figure 2.32: Absolute error over time between trajectory norm of Vicon and BB, in light color the singular trials, in dashed line the mean value. (+x).

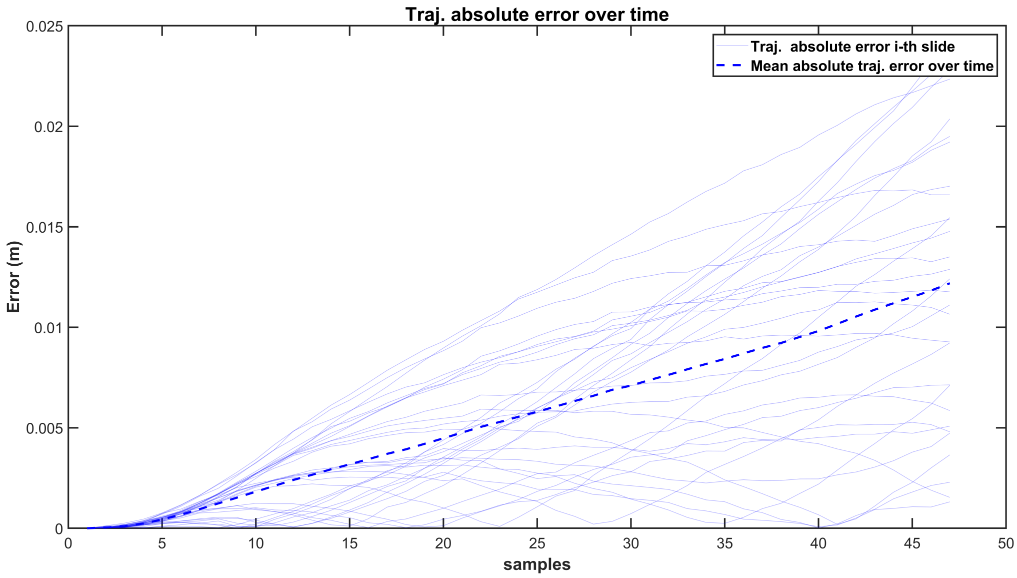

Figure 2.33: Absolute error over time between trajectory norm of Vicon and BB, in light color the singular trials, in dashed line the mean value. (-y).

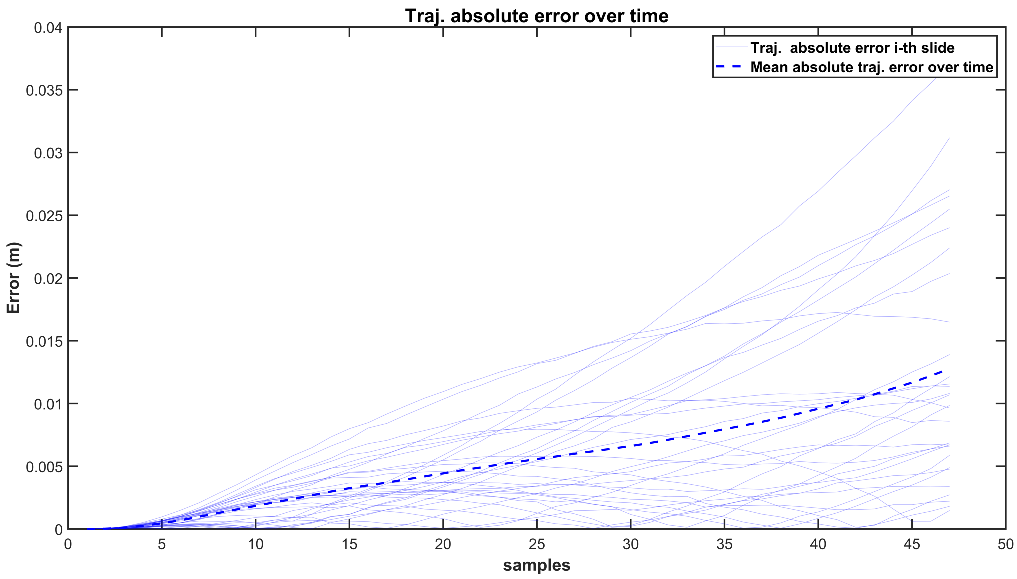

Figure 2.34: Absolute error over time between trajectory norm of Vicon and BB, in light color the singular trials, in dashed line the mean value. (+y).

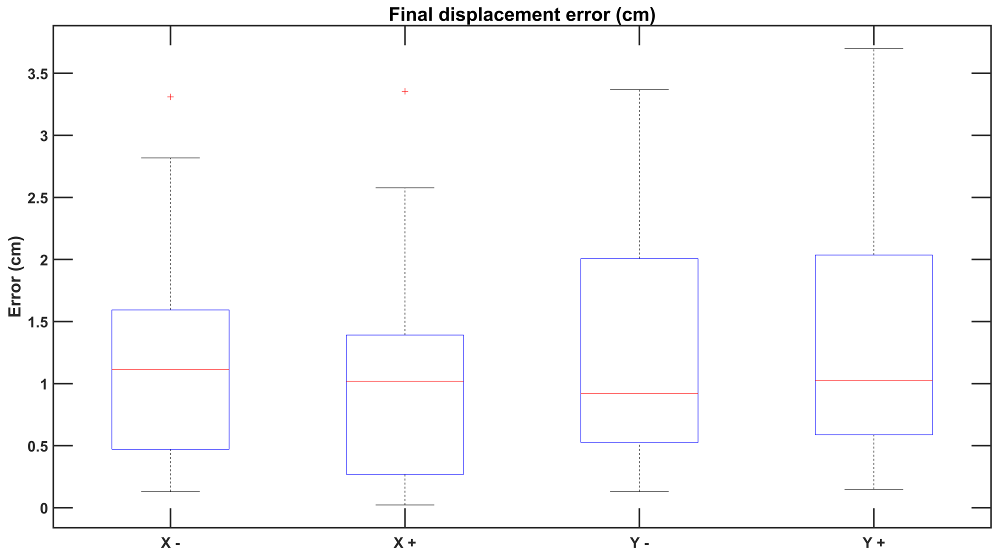

Figure 2.35: Mean absolute error over time distribution for each trial. (final displacement trajectory norm).

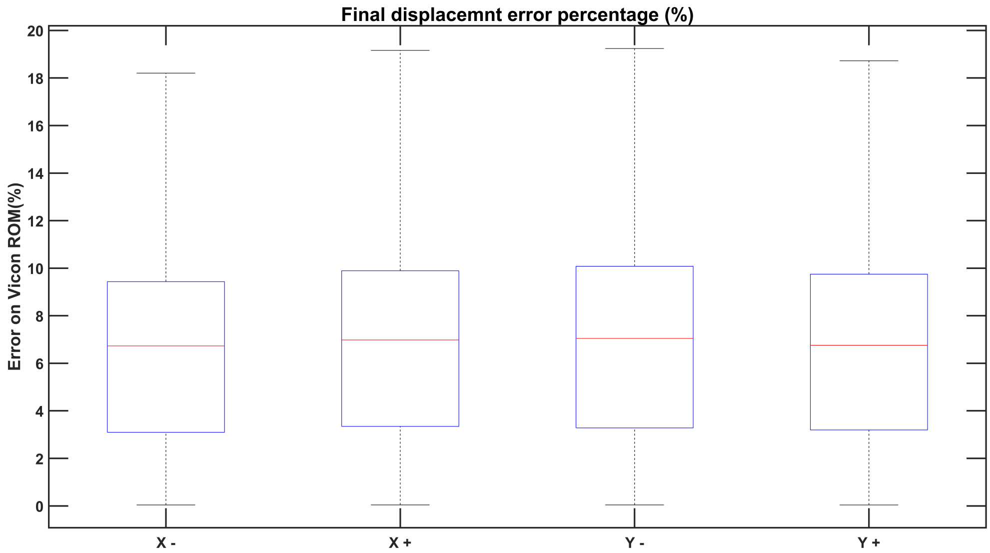

Figure 2.36: Mean absolute error over time distribution for each trial normalized for range of motion calculated on Vicon. (final displacement trajectory norm percentage).

2.5 Discussion

This first experiment had the aim of understanding the feasibility of a trajectory reconstruction using a single IMU, in controlled conditions. As proven by statistical test in previous section, the BB shows performance in final displacement estimation not statistically different than the gold standard. Final absolute displacement errors are around 1±0.7 cm for each axis, with a percentage of error around 6±4% to the Vicon movement. Errors on similar trials for commercial use devices, such as Xsense, over small time windows are about 1-2% of ROM[40]. Although less precise than other more advanced techniques, the assessments were made to investigate the error when direct double integration is directly applied. These increase in error in using direct double integration could be justified as the results of direct double integration during higher velocities tests, if confronted with expected velocities during a rehabilitative task. In general as the movement speed increases, the velocity and displacement errors accumulate more rapidly. From absolute errors graph is possible to see how the error increases over time, as expected, by the summation of integration errors during the movement. The greater standard deviation respect to gold standard acquisition can be explained as the erroneous identification of the algorithm of the starting and ending points for the slide movement, for example if 5 samples are lost due to incorrect segmentation, at experiment acceleration of 3m/s^2 and sampling frequency of 100 Hz, an error of almost 4 mm occurs on slide axis. Further analysis for improving the accuracy of the results are beyond the aim of this first experiment. Overall the trajectory estimation seems close to the gold standard if mean values are considered; the lack of higher precision could be compensated by averaging different trials in repetitive task, this makes think that could be possible reconstruct trajectory in more complex, but repetitive tasks such as R2G, and by employing different strategies to improve the estimation.

Chapter 3

Trajectory reconstruction using double integration and mechanical constraints on R2G

3.1 Introduction

As discussed in the previous sections, it is possible to reconstruct a trajectory with acceptable accuracy using a BB in simpler tasks, with errors around 6% of the total movement when applying direct double integration. This section explores how trajectory reconstruction can be improved by incorporating case-specific constraints into a R2G task, performed on eleven healthy subjects. The process begins with an initial estimation using double integration. From this baseline, a ZUPT approach is applied by identifying static periods during task execution. Finally, an optimization-based approach is introduced, leveraging problem-specific constraints to further refine the trajectory. Error assessment is conducted by comparing the estimated trajectory, derived from inertial data, with the gold standard trajectory. The absolute error is computed as the difference between these two trajectories over time. Additionally, percentage errors are calculated by normalizing the absolute error against the Range of Motion (ROM), defined as the difference between maximum and minimum displacement in the movement. R2G is a common exercise used to assess the functionality of ADLs and frequently used for clinical evaluations; the task consists of four movement phases as shown in fig. 3.1. This standardized sequence of movements provides a repeatable and structured approach for analyzing a functional, real-life action, such as reaching for a bottle of water to drink. Standardization enhances repeatability, ensuring a more stable and consistent evaluation of motor performance and enabling reliable comparisons between different patients performing the same task.

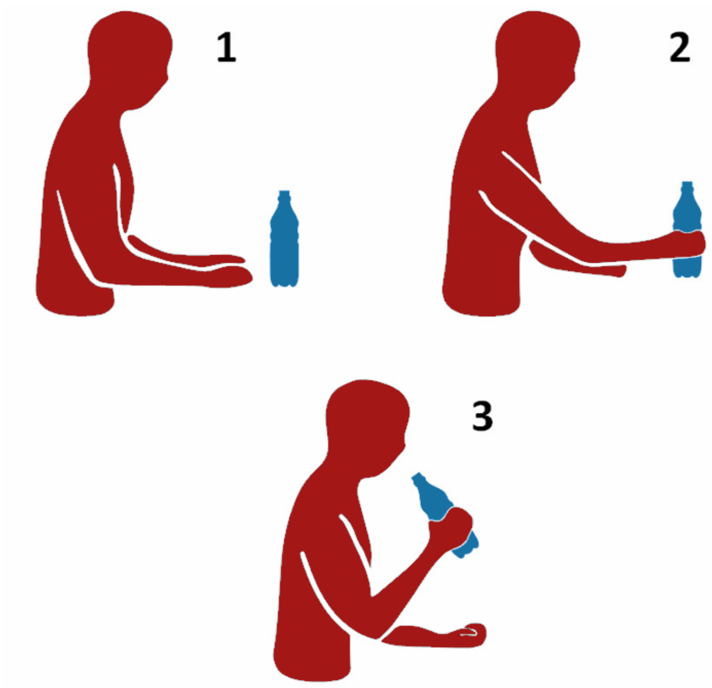

Figure 3.1: Schematic representation of drinking task. (1) The subject starts in static position with his hand on the table. (2) After a certain period of time, the subject execute a forward reach and grasping of the bottle (R2G). (3) After a certain period of time the subject bring the bottle to the mouth, simulating a drinking movement. Then the movement are repeated, with static period between each movement, in backward order from 3 to 2 and then from 2 back to 1.

3.2 Materials

3.2.1 Dataset and protocol

The data used for following methods were provided by Politecnico di Torino, during the study [41]. Only part of the data retrieved during acquisitions of the protocol were made available. The dataset consists of inertial data and corresponding gold standard acquisitions for eleven healthy subjects, three trials for each subject, during a R2G task. Subjects were required to perform a drinking task while sitting at a table (70 cm height), 30 cm distance from the table, with dominant hand. The bottle was positioned 1.5 times the forearm length from the table's edge. The task consisted of four phases, a schematic representation is shown in fig. 3.2 :

- Reach and grasp of the bottle (Phase 1)
- Lift of the bottle to simulate drinking (Phase 2)
- Return of the bottle on the table (Phase 3)
- Return of the hand to starting position (Phase 4)

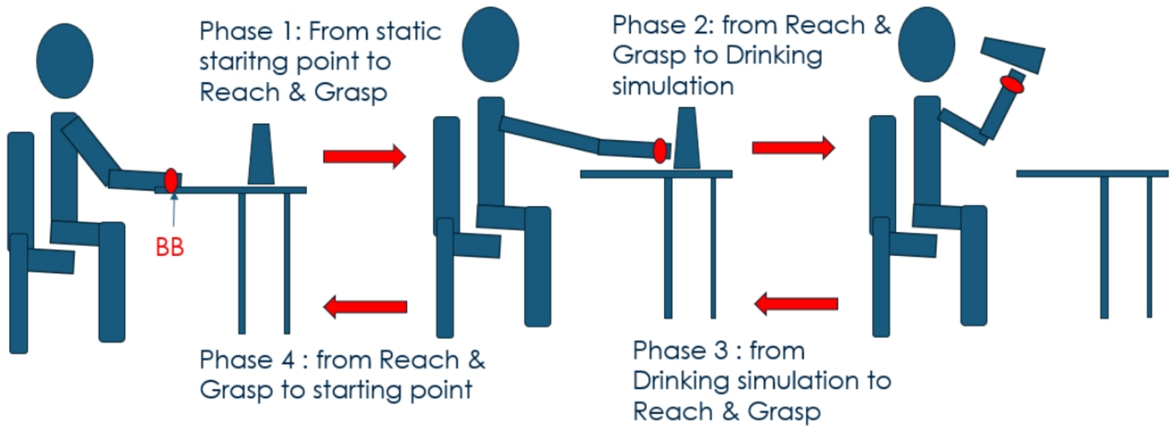

Figure 3.2: Schematic representation of each phase of the drinking task during the protocol acquisition.

Between each of these a static period of about four seconds was observed. For each trial, 25 drinking movement were performed, for a total of 825 total movements (25 tasks x11 subjects x3 trials). Inertial data were recorded by using BB positioned on the wrist, as in fig.. 3.3, the gold standard was recorded with the same stereophotogrammetic system described in the previous experiment, using four reflective markers mounted on BB, (Vicon T20, Vicon Motion Systems, Yarnton, Oxfordshire), recorded in the Motion Analysis Laboratory of PolitoBIOMed Lab, Politecnico di Torino (Turin, Italy).

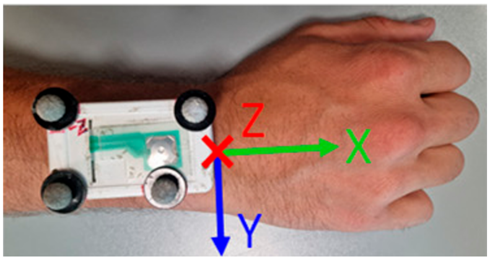

Figure 3.3: Setup and orientation of reference system of the BB during the protocol. Images source [41].

In fig. 3.4 is displayed the trajectory estimated by using gold standard, represented as relative displacement from the starting position.

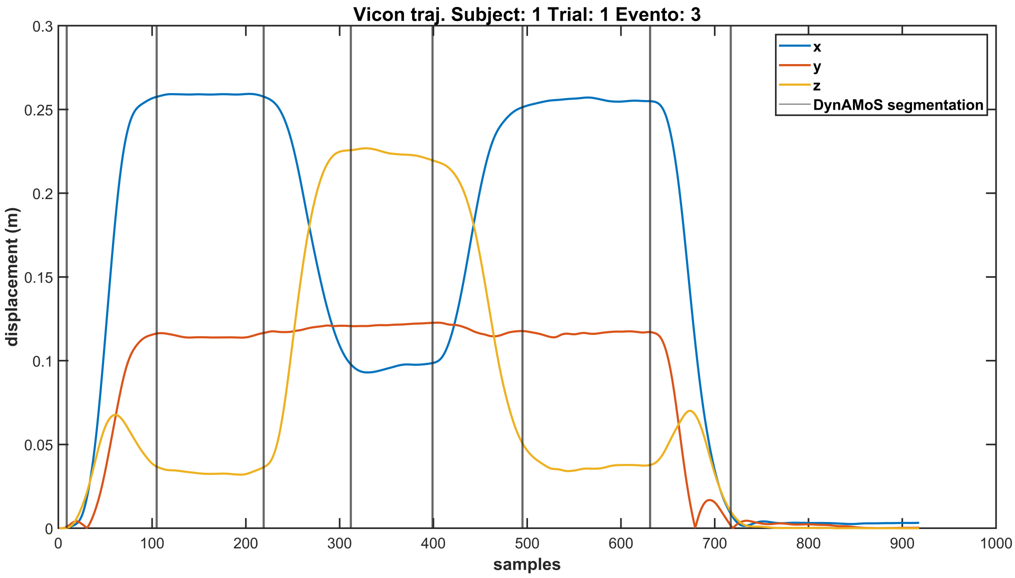

Figure 3.4: Example of Vicon signal for an execution of 4 phases R2G, along DynAMoS segmentation movement identification.

In fig 3.5 are also highlighted the four dynamic phases alongside Vicon signals.

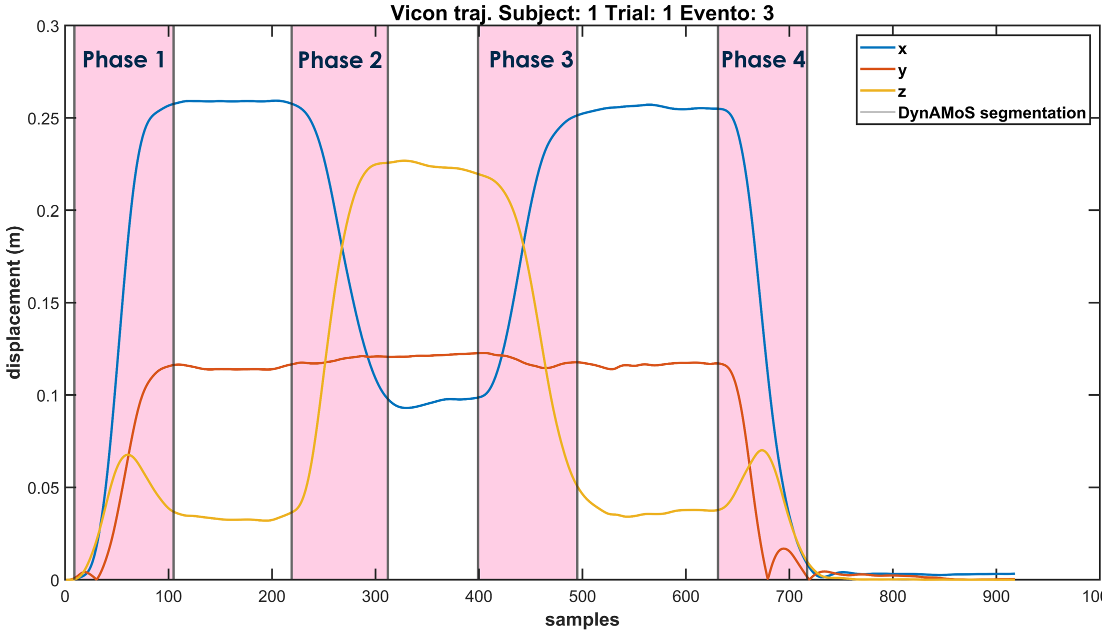

Figure 3.5: Example of Vicon signal for an execution of 4 phases R2G with each phase highlighted. During phase 1 and 4 most of the movement happen on transverse plane (x,y), while during phase 2 and 3 mostly on sagittal plane (x,z).

3.2.2 DynAMoS algorithm

For identifying static and dynamic phases it is used the algorithm by Dotti in [41], which proposes a new method for identification of dynamic phases in R2G tasks, with a single inertial unit positioned on the wrist. This method, (DynAMoS) uses an adaptive threshold on norm of the angular velocity, retrieved from gyroscope, and a statistical based post processing to reduce the number of erroneous identifications. The threshold is found by using Otsu's method, as a fraction of the angular velocity norm, identifying voluntary movement onset and offset to maximize the inter-class variance. Two thresholds are set using two parameters α and β, the first identifies movements that are too short, and thus considered artifacts, and the second identifies movement that are too long, i.e. formed by the merging of two phases that need to be split. A post processing based on statistical consideration is then applied to remove or merge false instants identifications. When the combined duration of short movements with adjacent ones is within normal limits, the phases are merged, if the duration of long movements are at local minima in the angular velocity norm, the phases are split. The process is iterative and is repeated until all movement durations fall within acceptable limits.

3.3 Methods

All following processing described in this section were achieved by using MATLAB r2023b software (MathWorks Inc., Natick, MA, USA). A schematic flowchart of the methods is presented in fig. 3.6.

First, the DynAMoS algorithm was applied on angular velocities retrieved by the IMU during the task execution, the 25 R2G movements were performed consecutively, and so they were first separated. Then, dynamic phases were located by using DynAMoS algorithm. However, in some tasks more than four phases were identified, possibly by a wrong execution by the patient. These extra-phases were corrected by evaluating features of duration, heights and distances on the corresponding subject, on task in which all the four phases were correctly identified. All R2G tasks were considered and processed singularly.

Using Valenti method [42], an initial estimation of the orientation of the system was calculated , by using the acceleration and angular velocity in the static period previous to the task, identified using a threshold of 0.1 rad/s on the norm of angular velocity. This method uses quaternions to express changes in orientation because they are a more accurate representation and do not incur a singularity state, unlike Euler's angles.

A Madgwick filter [34], is then applied using the previous orientation estimation, to combine the gyroscope and accelerometer data and compute quaternions orientation of the R2G. From there, the rotation matrix is extracted and used to convert the acceleration from local reference system from on the IMU to the global reference system. Gravity contribute is then removed by removing the mean value of the acceleration during the R2G task.

The trajectory reconstruction was first evaluated by directly performing a double integration of the corrected acceleration over the R2G task.

A second evaluation was conducted using a ZUPT approach, in which the acceleration was integrated once while enforcing a zero-velocity constraint during static phases outside of the DynAMoS segmentation. A final integration step was then performed to obtain the trajectory.

Lastly, the ZUPT-based trajectory was refined through optimization, using it as an initial estimate. Constraints were imposed based on protocol measurements to ensure accuracy. Specifically, a reference trajectory was defined considering the initial hand-to-bottle distance, the initial hand-to-sternum distance, and the mouth height relative to the table.

The optimization process minimized a cost functional composed of multiple terms, which were selected based on performance in trajectory reconstruction through trial and error on a small samples of 20 random selected R2G tasks.

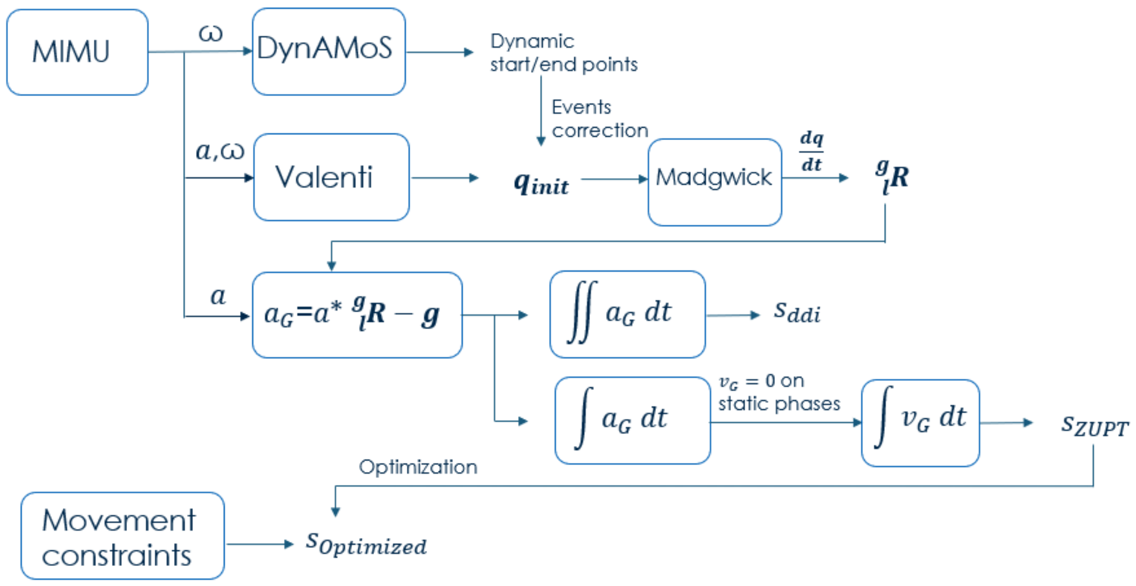

Figure 3.6: Flowchart of the methods for the experience. First, DynAMoS segmentation points are extracted and corrected by removing extra detected events. Through [42], using acceleration and angular velocity data from the IMU, it is initialized the quaternion representing the initial orientation. A complementary filter [34] is then used to compute the rotation matrix at each time instant during the drinking task. The acceleration is expressed in the global reference frame and gravity is removed by subtracting the mean value. A first approximation of the trajectory is obtained through direct double integration (s_{ddi}). The trajectory is also estimated by setting the velocity to zero during the static phase before integration (s_{zupt}). Finally, an optimization process using movement constraints defined by the protocol further refines the trajectory estimation ($s_{\text{optimized}}$).

3.3.1 Events correction

While DynAMos segmentation algorithm reach good segmentation results for identification of start and end of a dynamic movement, compared to other state-of-the-art approaches [41], on some subjects, on some trials, possibly due to incorrect task execution, more than four phases are identified as seen in fig. 3.7.

To correct the segmentation result for events that show n phases (with n >4), it was employed a technique based on calculating for each subject a set of features for every phase:

- Durations: $D = \{d_1, d_2, \ldots, d_n\}$
- Heights: $H = \{h_1, h_2, \ldots, h_n\}$
- Distances: $S = \{s_1, s_2, \ldots, s_{n-1}\}$

These features were calculated for each subject on each event that showed exactly four phases, then for each subject it was calculated the mean value of each feature.

$$D^* = \{d_1^*, d_2^*, d_3^*, d_4^*\}, \quad H^* = \{h_1^*, h_2^*, h_3^*, h_4^*\}, \quad S^* = \{s_1^*, s_2^*, s_3^*\}$$

Eliminating the extra-phases requires to find the subset of four events that minimizes the root mean square (RMS) error:

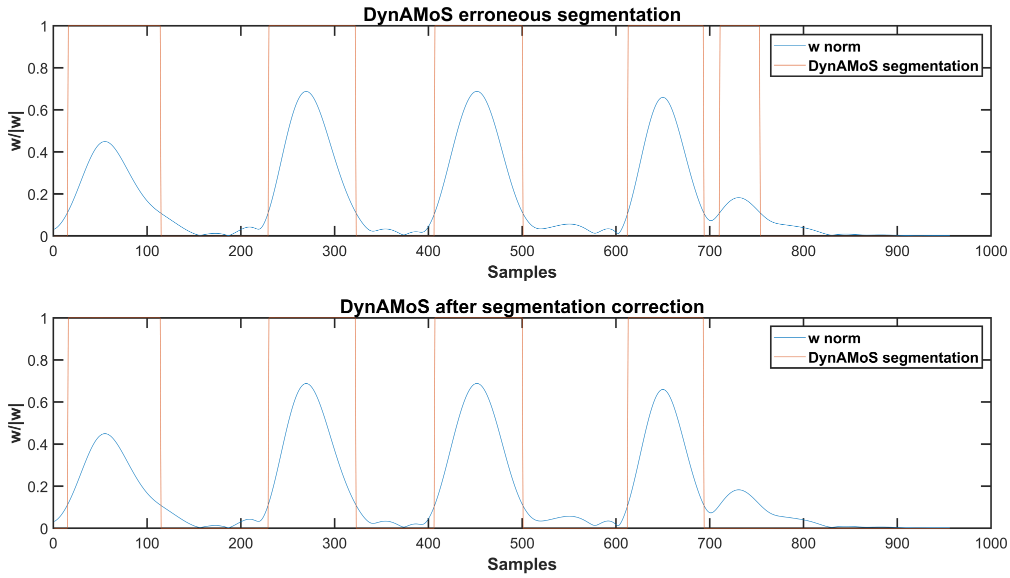

Figure 3.7: Example of DynAMoS wrong event identification in the figure above, and removal of extra phase by using events correction algorithm in figure below.

$$\{d_i^*, h_i^*, s_i^*\} = \arg \min_{\{d_i,h_i,s_i\}\subset\{d_j,h_j,s_j\}_{j=1}^{n-4}} \left(\sqrt{\frac{1}{4}\sum_{j=1}^{4}(d_j - d_j^*)^2} + \sqrt{\frac{1}{4}\sum_{j=1}^{4}(h_j - h_j^*)^2} + \sqrt{\frac{1}{3}\sum_{j=1}^{4}(s_j - s_j^*)^2} \right)$$

where: d_j, h_j, and s_j are the selected event features. d_j^*, h_j^*, and s_j^* are the reference values. The selection is made by iterating over all possible event combinations and choosing the one with the smallest error.

By doing so extra phases are found and removed, this ensure that latter algorithms and consideration based on phases identifications would work.

3.3.2 Task segmentation

After having retrieved inertial data, the entirety of the signal is separated in the 25 drinking task, each with the corrected four phases identification. This is done by calculating the norm of angular velocity and dividing the signal in segments corresponding to the duration of the task. First, non static instant are found by using a threshold on normalized angular velocity of 10% of the maximum value. Then is calculated the distance between each above threshold value. Candidates for end of a drinking task must be both separated by a long static period, as designed by the protocol, and have an above threshold value of angular velocity. End points are found as the first 25 more distant values of above threshold candidates.

Starting point for drinking task are found by considering the first above threshold candidates after an end of a task. In fig. 3.8, is shown an example of the separation of the signal in multiple drinking task.

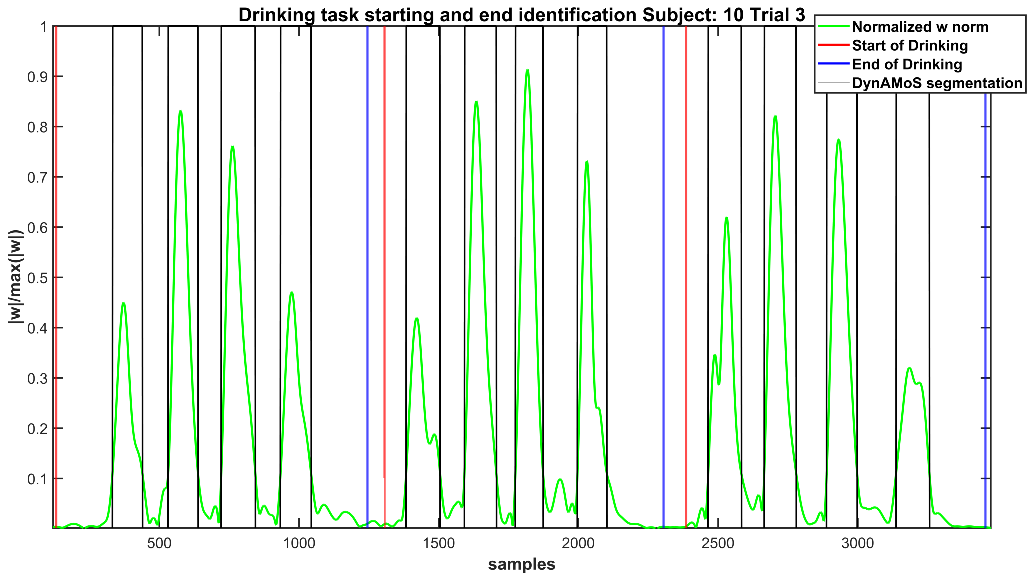

Figure 3.8: Example of drinking task segmentation (from red line to blue line), using angular velocity norm. In green angular velocity norm divided by its maximum value over all 25 trials, in black DynAMoS dynamic phase identification.

3.3.3 Orientation estimation

Then to proceed with any integration operation, is first necessary to evaluate the change in orientation during the movement. First, the initial orientation is estimated on the static period precedent to the task, identified by using a threshold of 0.1 rad/s on the norm of angular velocity from the previous end of drinking task to the first sample above average (for the first iteration the start of static is found as the first sample). The starting orientation is estimated using the mean of accelerations value during the static period, with quaternion estimation proposed by Valenti [42], which uses quaternion of acceleration to compute roll and pitch components and quaternion of the magnetometer to compute yaw component. Then, the Madgwick filter [34] is applied to compute changes in orientation relative to the initial estimated orientation during the drinking task. This variation is measured from the end of one static period to the start of the next. Magnetic field is not considered reliable over the dynamic period and thus only accelerometer and gyroscope data is used for the filter. As parameter β of the filter, is chosen 0.03, as it is the recommended value for dynamic performances. From quaternion estimation is computed the rotation matrix for each time instants of the dynamic part, necessary to rotate the reference system from starting position to global frame. Acceleration data is then rotated by multiplying for rotation matrix gravity is removed by removing mean value of acceleration along each axis during dynamic period, in fig. 3.9 is shown the acceleration rotated in the global reference system with gravity removed.

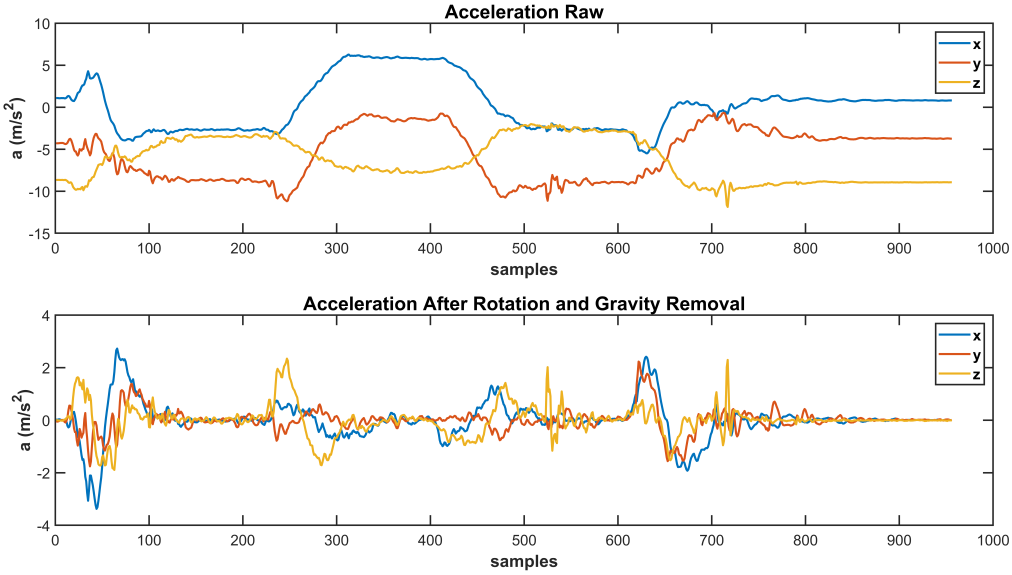

Figure 3.9: Example of raw acceleration over a single drinking task in the figure above, and after rotation in global reference system and gravity removal in figure below.

3.3.4 Double integration

The first approach used for trajectory reconstruction was double integration; as seen in previous experiment, this approach is not expected to give best results but it is a starting point to later improve performances. Integration operation is performed by using MATLAB integration method "cumtrapz" which employs trapezoidal formula for integral computation.

3.3.5 Zero velocity update

The direct double integration approach resulted in an expected imprecise trajectory estimation, with drift errors accumulating during integration. The presence of repetitive static phases during the task, inspired the application of a ZUPT method, typically employed with inertial data during gait analysis with an IMU mounted on the foot [28]. By knowing where the movement occurs, the integration is applied only during movement, while static phases are forced to have null velocity, thus reducing drift error as seen in [29]. Dynamic phases are identified by using DynAMoS corrected segmentation.

In fig. 3.10 is displayed an example of the approximation made by setting to zero velocity over static period by comparison of velocity over direct double integration and Vicon gold standard.

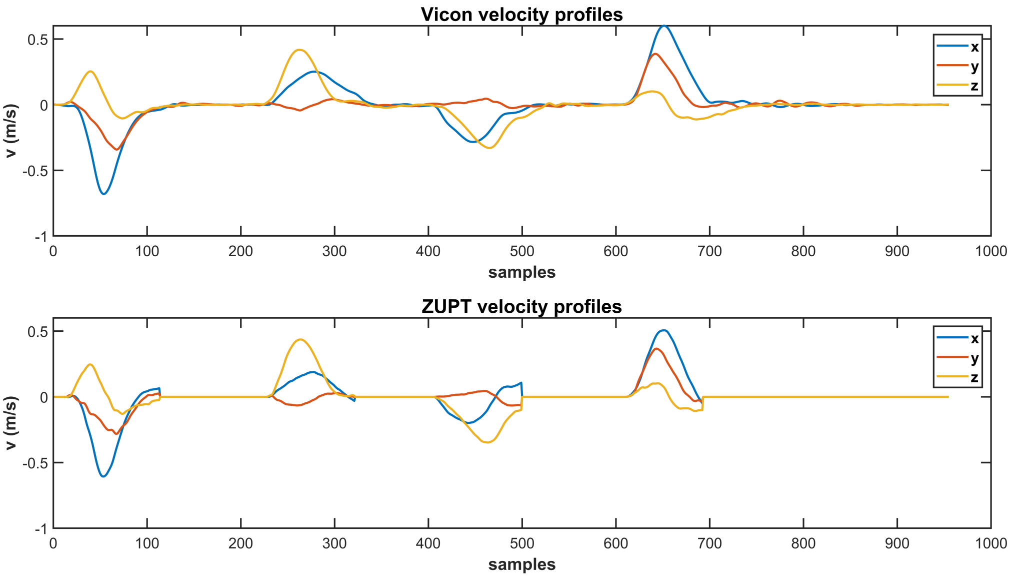

Figure 3.10: In the figure above: Vicon velocity profile obtained by derivating over time once. In the figure below: ZUPT velocity profile by integrating once the corrected acceleration and forcing null velocity in static phases.

3.3.6 Optimization

Although showing better results than direct double integration, ZUPT approach still shows residual error, mostly consisting in drift cumulated at the end of the signal; a new method is proposed to get closer to gold standard results, by defining an optimization problem with function cost and constraints that uses case-specific characteristic of the expected trajectory. As requirement for an optimization problem, there is the definition of a cost function; this should be described so that when the optimization algorithm converges, the solution is closer than the initial guess to the desired signal. To investigate which functional costs are more adequate to improve the results, each cost functional, is first calculated for both Vicon and ZUPT on 100 random trajectories and then compared. If the value of a cost functional differs significantly when computed using the gold standard trajectory compared to the ZUPT trajectory, it indicates that the functional is suitable for inclusion in the cost function definition. By observing the expected trajectory characteristics, the following cost functional are defined and computed and represented as distributions:

- **Symmetry** The protocol defines a periodic task to be performed with regular pauses between each dynamic movements, so it is reasonable to expect the trajectory to be symmetrical. Two symmetry cost functional are defined; the first is defined as the difference of the signal starting from the start of the first dynamic movement (phase 1) to the end of the last dynamic movement (phase 4), found by DynAMoS (3.1). The second uses the same considerations made but uses phase 1&4 and 2&3 coupled, as in(3.2).

$$\text{symmetry\_cost} = \frac{1}{l} \sum_{t=\text{starts}(1)}^{\text{ends}(end)} |s(t) - s(l-t)| \tag{3.1}$$

Where "starts" and "ends" are the time samples identified by DynAMoS corresponding to start and end of a phase, "l" is the duration of the signal.

In fig. 3.11 and 3.12 are shown comparisons in symmetry between Vicon and ZUPT.

$$\text{coupled\_cost} = \frac{1}{l}\left(\sum_{t=\text{starts}(1)}^{\text{ends}(1)} |s(t) - s(\text{ends}(4) - t)| + \sum_{t=\text{starts}(2)}^{\text{ends}(2)} |s(t) - s(\text{ends}(3) - t)|\right) \tag{3.2}$$

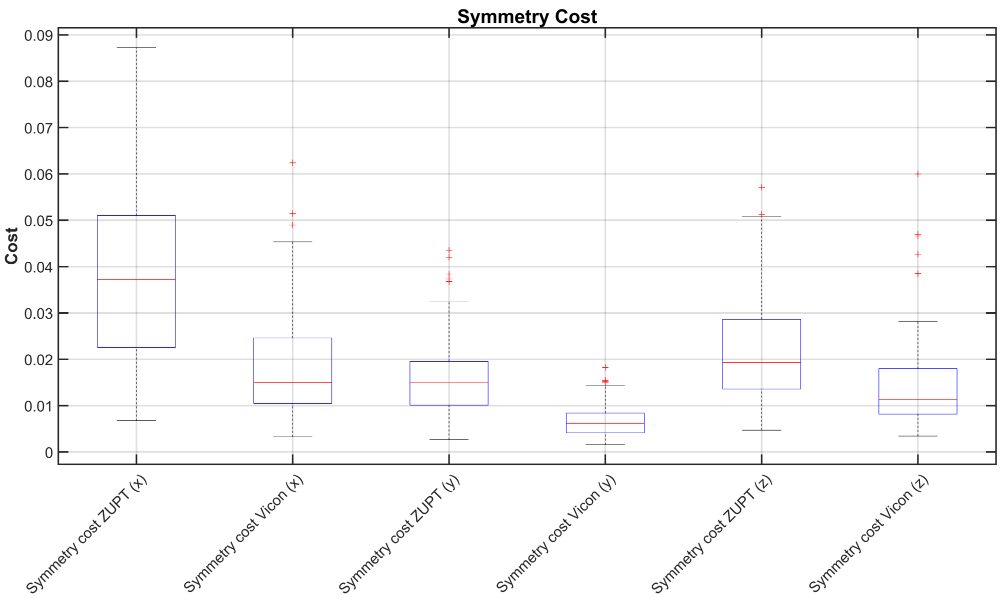

Figure 3.11: Symmetry functional cost value for Vicon and ZUPT approach, for each axis over 100 random trajectories.

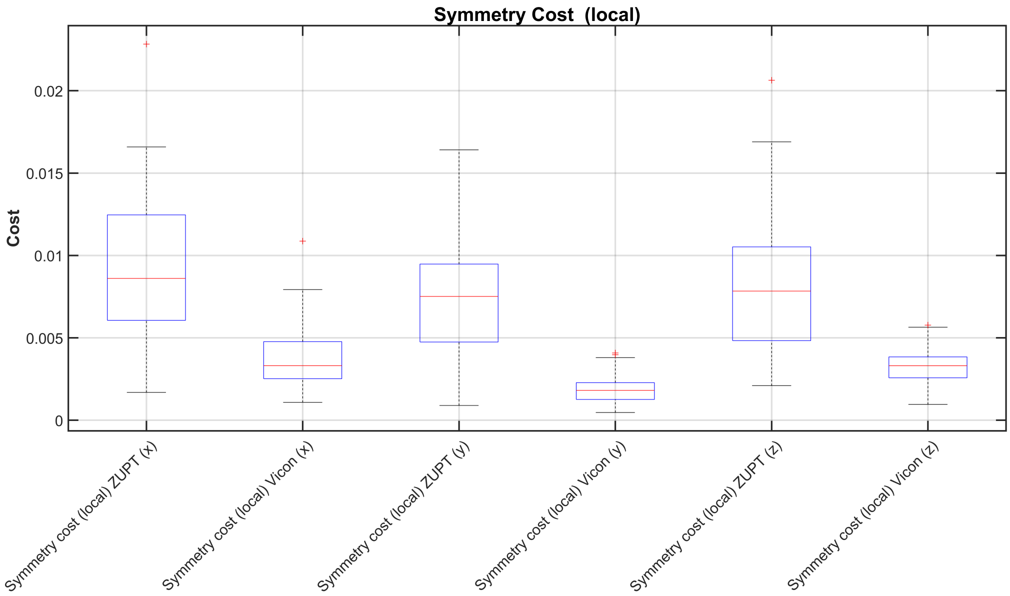

Figure 3.12: Symmetry local functional cost value for Vicon and ZUPT approach, for each axis over 100 random trajectories.

- **Jerk** Jerk is described as the derivative of acceleration; human motion is characterized by efficient movement, in fact among all possible trajectories that can be selected to achieve a certain movement, in healthy subjects, the one most likely to be chosen by the central nervous system is the one more fluent and minimal jerk [43]. For these reasons jerk is defined only on dynamic phases as in (3.3). In fig. 3.13 is shown the comparison in jerk between Vicon and ZUPT.

$$\text{jerk\_cost} = \sum_{i=1}^{4} \frac{1}{\text{ends}(i) - \text{starts}(i)} \sum_{t=\text{starts}(i)}^{\text{ends}(i)} \left| \frac{d^3}{dt^3} s(t) \right| \tag{3.3}$$

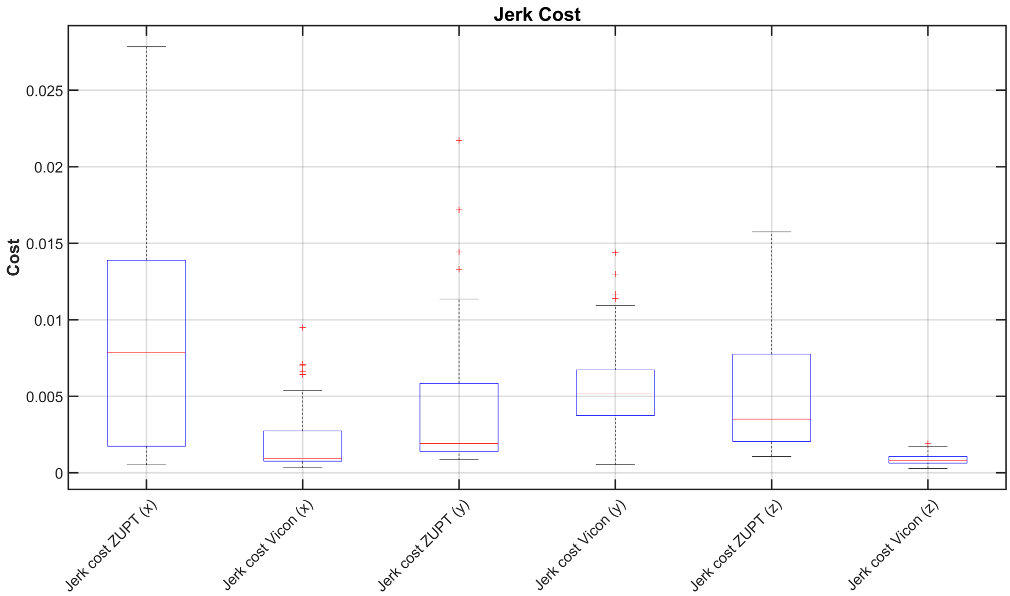

Figure 3.13: Jerk local functional cost value for Vicon and ZUPT approach, for each axis over 100 random trajectories.

- **Energy** Also energy contribution were analyzed to discover significative differences; by observing some trials seems that ZUPT estimations tend to underestimate the expected trajectory. Energy cost is defined as in (3.4). In fig. 3.14 the comparison in symmetry between Vicon and ZUPT.

$$\text{energy\_cost} = \frac{1}{l} \sum_{t=\text{starts}(1)}^{\text{ends}(4)} (s(t))^2 \tag{3.4}$$

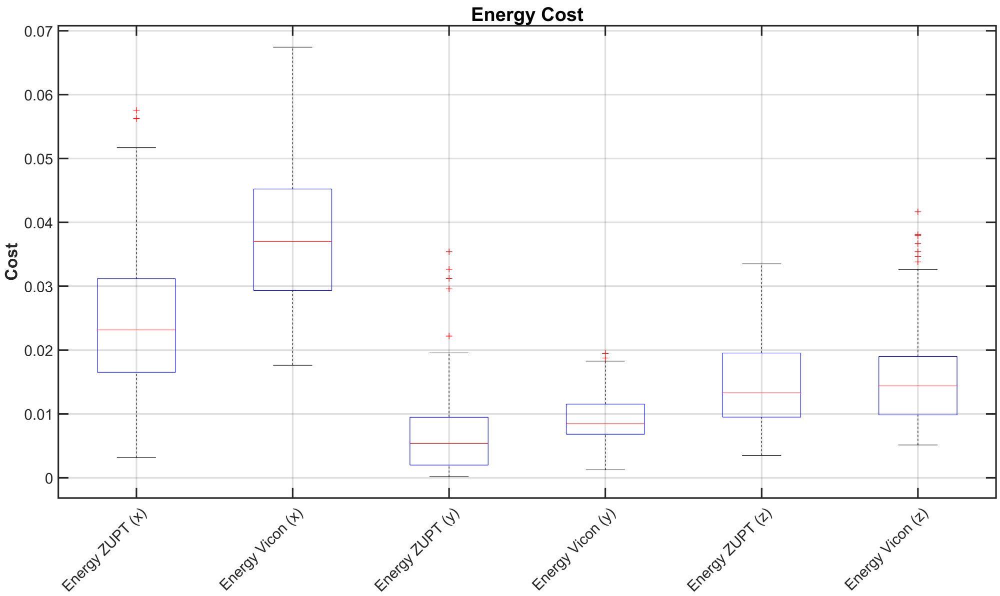

Figure 3.14: Energy local functional cost value for Vicon and ZUPT approach, for each axis over 100 random trajectories.

- **Smoothness** The movement is also suspected to show low to null velocity during static phases, so a smoothness cost was defined as (3.5). In fig. 3.15 the comparison in symmetry between Vicon and ZUPT.

$$\text{smoothness\_cost} = \sum_{i=1}^{4} \frac{1}{\text{ends}(i) - \text{starts}(i)} \sum_{t=\text{starts}(i)}^{\text{ends}(i)} \left| \frac{d}{dt} s(t) \right| \tag{3.5}$$

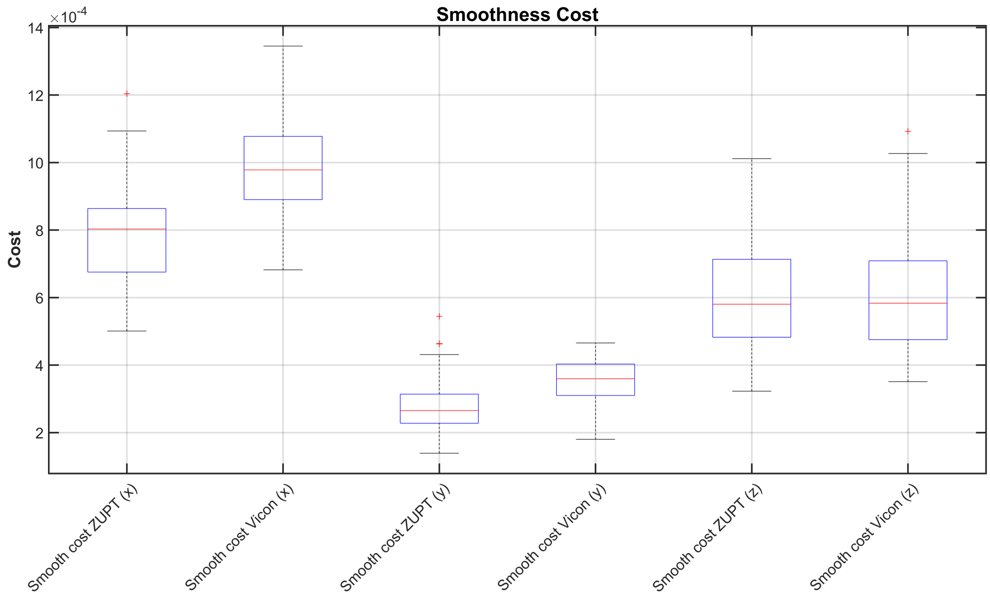

Figure 3.15: Smoothness local functional cost value for Vicon and ZUPT approach, for each axis over 100 random trajectories.

3.3.7 Constraints

Constraints were defined by taking into account the protocol definition and the feasibility of it from distance with simple measurement and easy set up. The idea is that by taking few measurements, is possible to constrain the volume in which the hand could move; for example, by measuring the length of arm, forearm, the distance from the staring position of the hand and the sternum, and the height of the mouth respect to the table, the volume in which the hand could be found at any time instants during the task-execution is bound. Another observation is that cumulating error over integrations, causes the final displacement to drift instead of returning to zero, so a constrain over this condition is also set. As seen in [33] or [44], optimization based solution rely on minimizing a errors between estimated position and expected reference position. In this case reference trajectory is used to enforce the constraints of the antropometrical measurements. Not having the direct measurements, they were obtained by calculating mean of displacement of Vicon reference for each subject as follows:

- h1: Distance of the bottle from the starting point of the hand along the frontal direction (x axis).
- h2: Distance from the sternum to the shoulder in the sagittal direction (y axis).
- h3: Height from the table to the mouth in the vertical direction (z axis).

Then each axis of the reference trajectory was defined according to the protocol description. The movement along x-axis starts from null movement, reach h1 at the end of phase 1, decreases after phase 2, then comes back to h1 at the end of phase 1 and finally return to the starting point at the end of phase 4. Along y axis the movement is more variable, but generally after phase 1 up to phase 4 stays around h2 and then comes back to starting position. Along z axis after phase 1 there is a slight variation from the starting position, after phase 2, during the drinking task,h3 is reached, then back to the slight variation from the starting position after phase 3 and to the starting point at the end of phase 4. For defining movement during the dynamic phases it was used Hoogan's model, which describes human movement transition as a fifth order polynomial [43]. An example of reference trajectory obtained along with Vicon reference is shown in fig. 3.16.

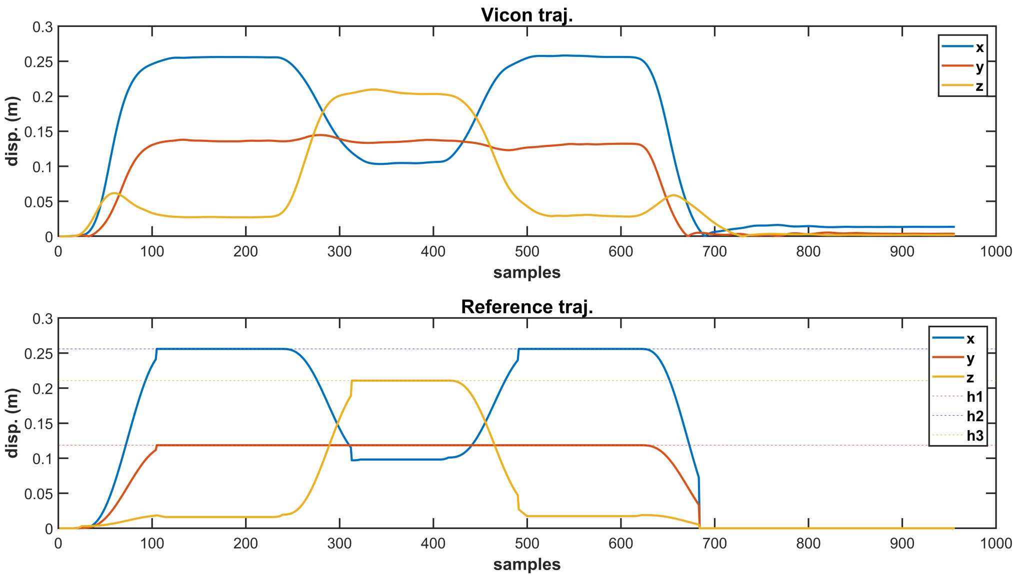

Figure 3.16: On top Vicon gold standard trajectory, at the bottom reference trajectory defined to enforce anthropometric constraints during static phase, dynamic phases are defined using Hoogan's model [43].

To determine the optimal combination of functional contributions for the reconstruction process, tests were conducted on only a subset of 20 randomly selected trajectories, due to the large volume of data and the high computational cost of processing a single trajectory.

The selection process involved visually inspecting the reconstructed trajectory against the gold standard and evaluating the norm error over time, ultimately choosing the best-performing contributions.

The selected contributions, which demonstrated superior performance, include:

- Coupled symmetry
- Smoothness
- Error respect to reference trajectory.

Additionally, non-linear constraints were imposed to ensure the trajectory returns to its starting position. For this final set of functional cost all R2G movements were examined.

Optimization was done using using MATLAB built in "fmincon" function, used for constrained nonlinear optimization, which finds the minimum of a scalar function while considering constraints. Interior-Point algorithm method was employed to solve the optimization problem, with 200 set as maximum number of iterations.

3.4 Results

A comprehensive summary of the errors obtained, using the discussed approaches, is reported in table 3.1.

Table 3.1: Error and Standard Deviation Results

	mean ± std (cm)			mean ± std (%)		
	x	y	z	x	y	z
ddi	15±9.4	14±9.1	4.0±2.8	51±32	47±30	13±9.1
ZUPT	4.9±2.7	3.9±1.5	2.0±0.9	16±9.4	13±5.0	7.1±3.0
opt	2.0±1.2	1.2±0.72	1.4±0.71	6.7±4.0	4.3±2.4	4.8±2.5

In the table, the mean absolute errors distributions and errors distribution as a percentage of ROM for all discussed approaches are shown. The results are presented as mean value ± standard deviation for each axis of the movement. Subject 6 was considered an outlier as discussed in the next section. std: standard deviation; ddi: direct double integration approach; ZUPT: zero velocity update approach; opt: optimization approach.

Using direct double integration, the mean absolute errors exceed 10 cm for the x and y axes, while remaining below 5 cm for the z axis. The ZUPT approach reduces errors to approximately 5 cm on the x-axis and under 4 cm on the y and z axes for most subjects. Finally, with the optimization approach, errors remain below 2 cm on all axes for all subjects.

For the direct double integration approach, errors exceed 50% of ROM on the x and y axes, while remaining around 15% for the z-axis. The ZUPT approach improves these values, reducing errors to approximately 15% on x and y axes and less than 10% on the other z axis. Finally, the optimization approach further reduces errors, keeping them below 10% for the x-axis and under 5% for the y and z axes in most cases.

Figures 3.18 through 3.20 show the mean absolute error distributions over time along each axis, for each subject, for each of the previously described methods. The error distribution is computed as the absolute difference between the Vicon reference and the corresponding method. These absolute errors are then averaged for the same axis and subject.

Figures 3.21 through 3.23 represent these errors as a percentage of the ROM, measured by the corresponding Vicon axis. This is obtained by dividing the previously computed errors by the mean ROM value of the respective Vicon axis.

Figure 3.17 presents a graphical comparison of trajectory reconstruction for a single R2G. From top to bottom, the figure displays the Vicon reference trajectory, direct double integration, ZUPT, and optimized trajectory.

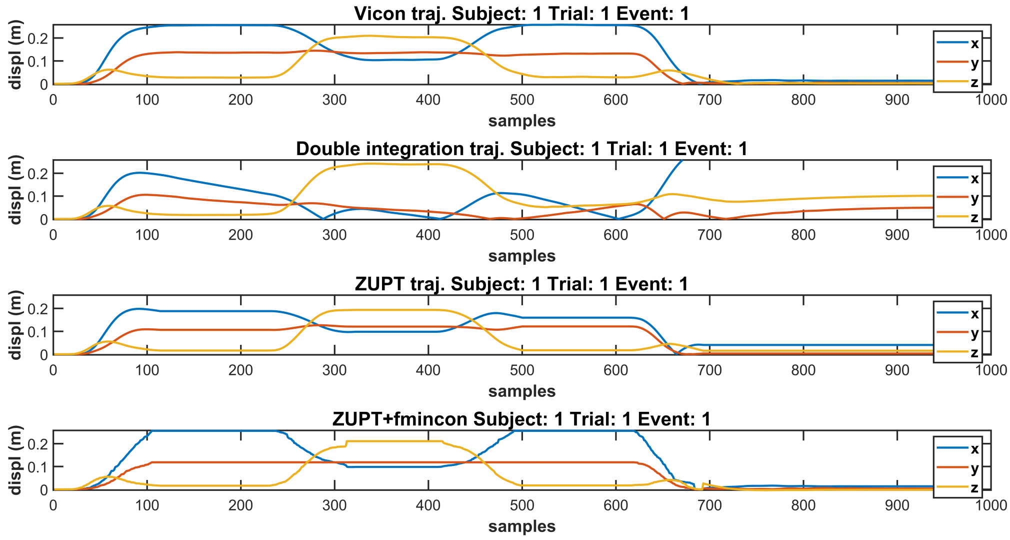

Figure 3.17: Example of trajectory reconstruction for a drinking simulation: from top to bottom, Vicon gold standard trajectory, direct double integration trajectory, ZUPT trajectory and optimized trajectory.

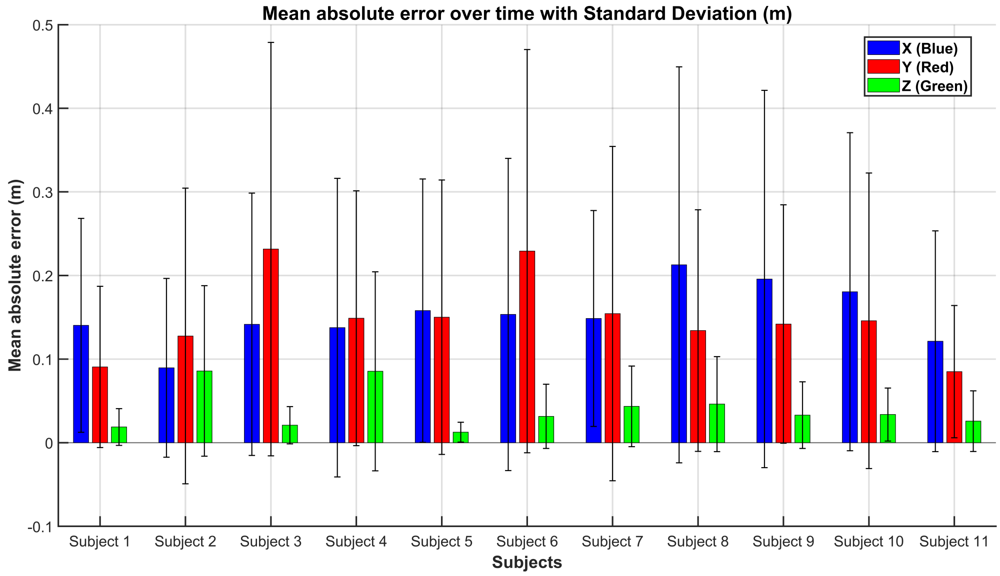

Figure 3.18: Mean absolute error distribution during drinking task for each subject along x,y and z axis. (From direct double integration).

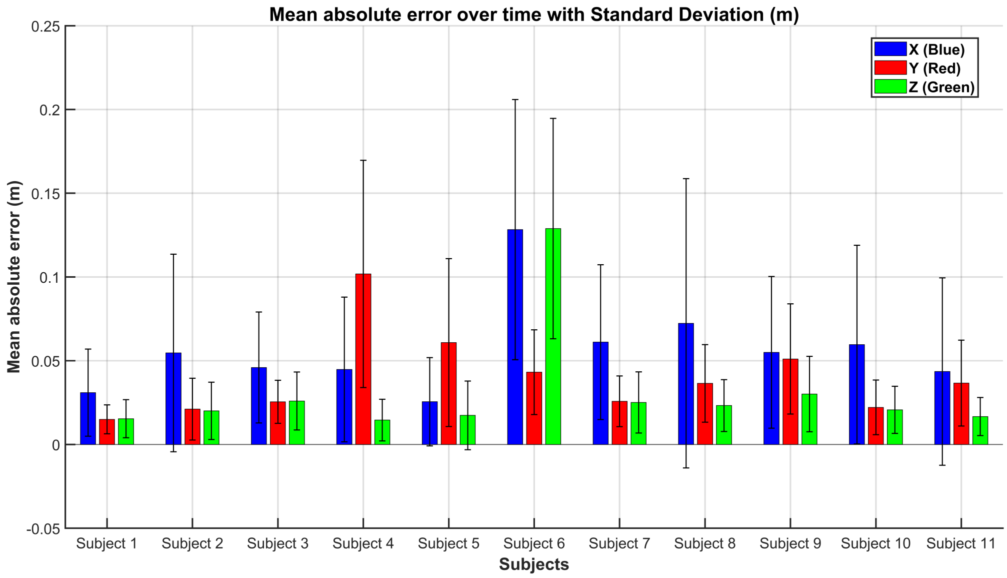

Figure 3.19: Mean absolute error distribution during drinking task for each subject along x,y and z axis. (Using ZUPT approach).

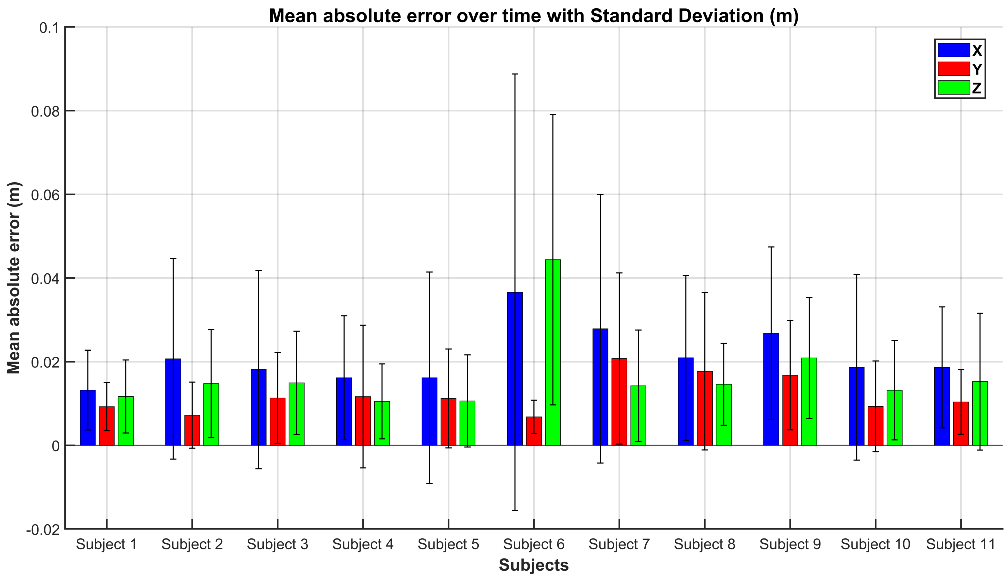

Figure 3.20: Mean absolute error distribution during drinking task for each subject along x,y and z axis. (Using ZUPT + optimization approach).

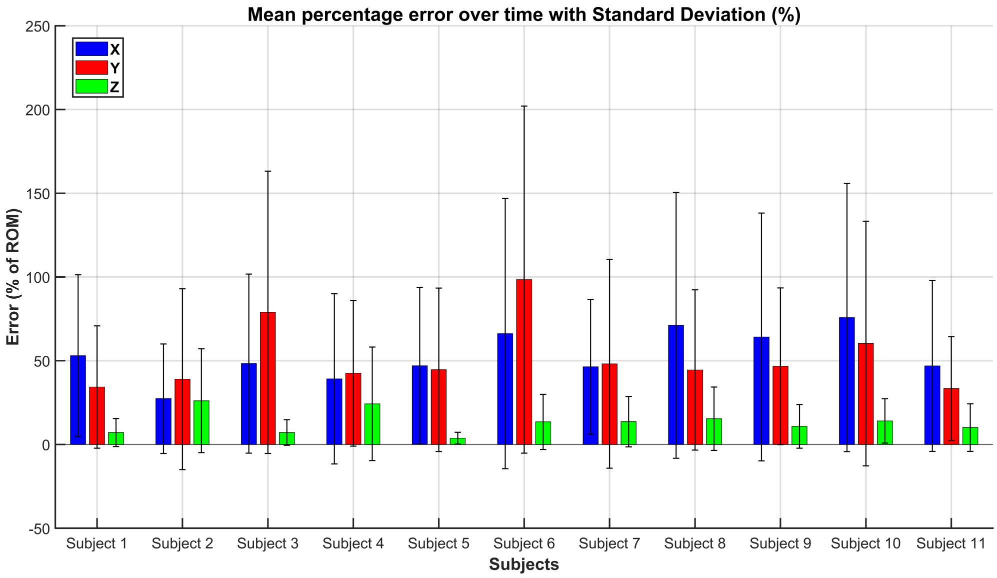

Figure 3.21: Mean absolute error distribution during drinking task for each subject along x,y and z axis, normalized for the Vicon range of motion.(From direct double integration).

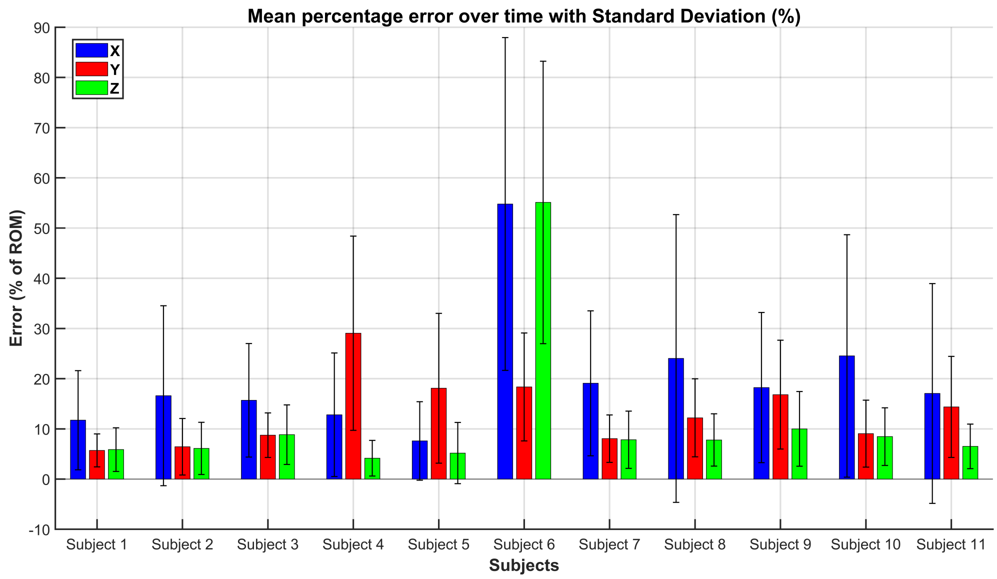

Figure 3.22: Mean absolute error distribution during drinking task for each subject along x,y and z axis, normalized for the Vicon range of motion.(Using ZUPT approach).

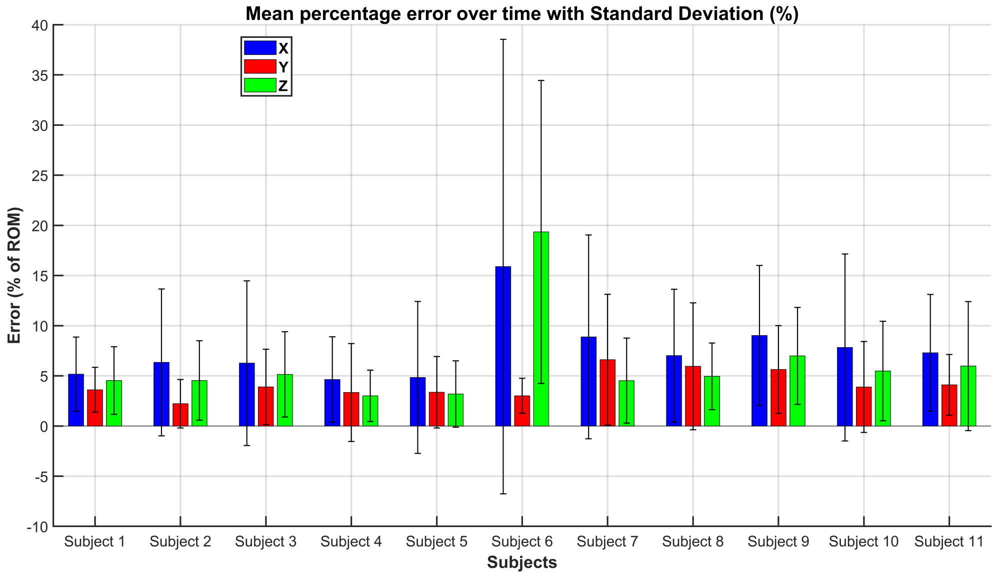

Figure 3.23: Mean absolute error distribution during drinking task for each subject along x,y and z axis, normalized for the Vicon range of motion.(Using ZUPT + optimization approach).

3.5 Discussion

In the final part of this work, a dataset of 11 healthy subjects data recorded from an IMU on wrist during drinking task simulation was analyzed. Different approaches were used to estimate trajectory over time for each drinking simulation, and validated against a stereophotogrammetric gold standard.

First a direct double integration approach was used, showing a great error and error dispersion over time for most subjects; around 15±10cm for x and y axis corresponding to an error on expected ROM of more than 50%, while a bit more precise on z axis around 10±5cm, corresponding to less than 10% of expected ROM. So, a ZUPT approach with DynAMoS phases identification was implemented to improve the results, by successfully reducing errors up to around 5±5 cm for x and y axis corresponding to 15% of expected ROM for most subjects, and less than 2±2cm for almost all subjects along z axis (5% or ROM).

Finally, an optimization method was developed, by combining different cost functional contributes and enforcing constraints on expected movement, to further reduce errors, resulting in errors for most subjects of around 2±2 cm on x-axis and less than 2±2 cm on y and z axes, corresponding to less than 10% on x-axis and around 5% on other axes.

The methods seems to have variable performance based on subjects, for example subject 4,6 and 8 show higher errors; this can probably be attributed to offset of phases identification, resulting in loss of information during double integration; For example, in fig. 3.24 and fig. 3.25, the ZUPT estimated trajectory for subject 6 shows a great underestimation in displacement, respect to a trajectory from subject 1, the hypothesis forced of null velocity in the static phases is in fact an acceptable approximation for subject 1 but not subject 6, who shows a residual velocity before and after DynAMoS identified phases.For these reasons, subject 6 was considered an outlier and not considered in the computation of final errors reported. This could be improved by reducing the norm velocity threshold used for starting and end point segmentation.

Typical trajectory estimation error on similar functional task, with similar velocities, have reached errors around 0.1 cm on 10 cm movement using kinematic models, or 0.8% errors of ROM movements [29].

These results shows that, at list on healthy subjects, a trajectory resembling the gold standard could be reconstructed, with errors over time of less than 10% of ROM after optimization; however by lacking data of patients affected by neuromuscular disorder of upper limb, is difficult to say how the methods would behave in these cases. By having less fluid and more uncertain movements many functional costs used for optimization such as symmetry and jerk, may no longer be suitable for describing trajectory, thus resulting in a less accurate trajectory. Also the protocol expects the patient to reach certain range of movements, this could be not possible in case of greatly compromised upper limb functionality. Overall, the methods should be tested on patients and, in case of poor performances, constraints should be relaxed or functional cost should be changed.

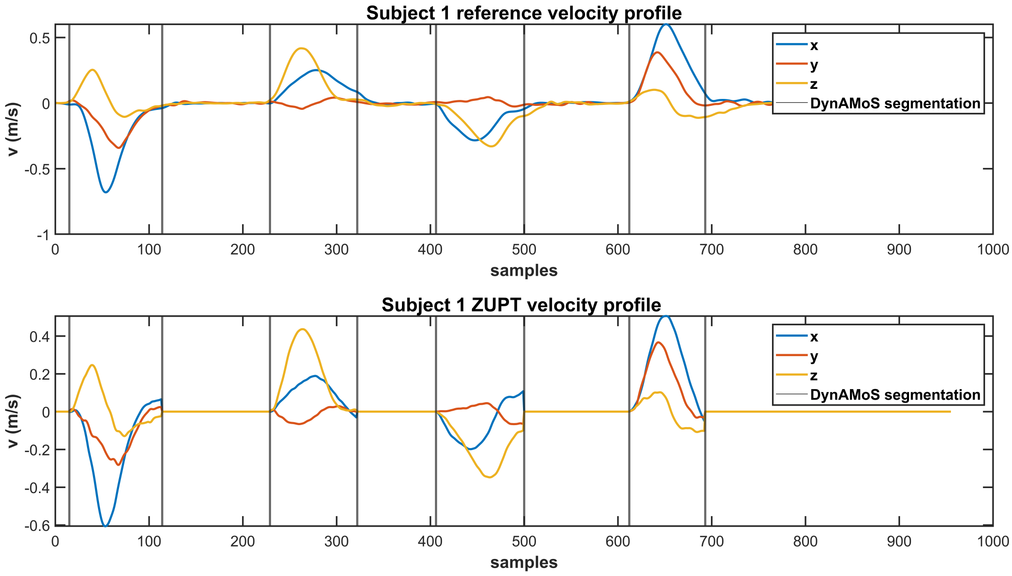

(a) Velocity profile of Vicon (above) and from ZUPT approach (below) for subject 1

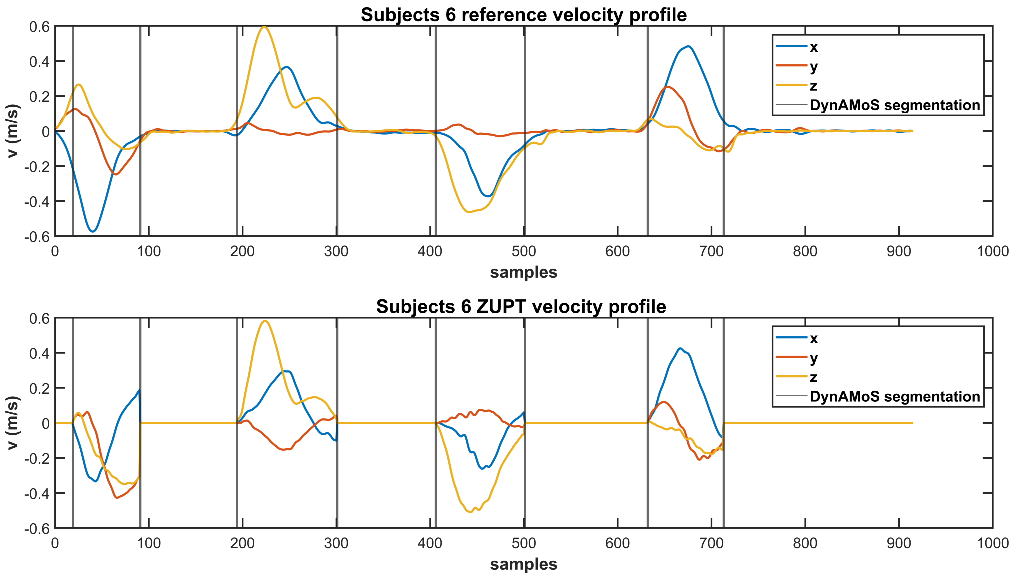

(b) Velocity profile of Vicon (above) and from ZUPT approach (below) for subject 6

Figure 3.24: Velocity profile using ZUPT approach for subject 1 (a) and 6 (b) compared with reference profile obtained by Vicon data.

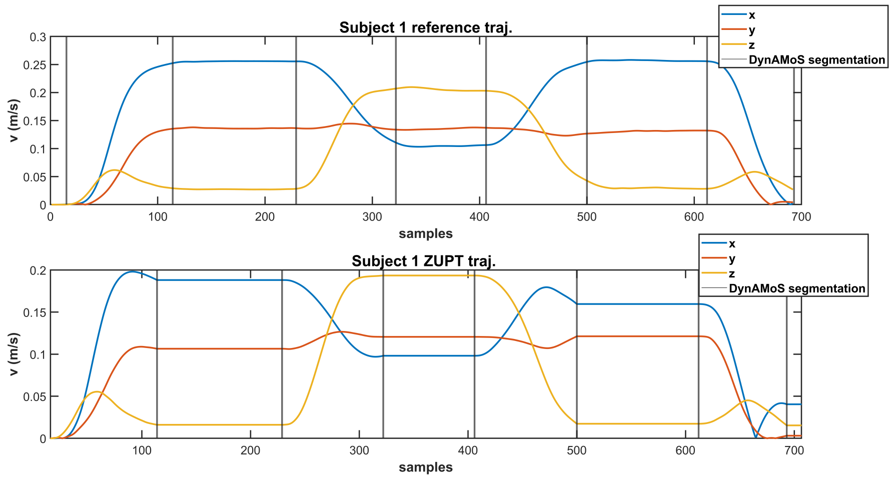

(a) Trajectory obtained with good approximation of velocity profile (below) against gold standard trajectory (above).

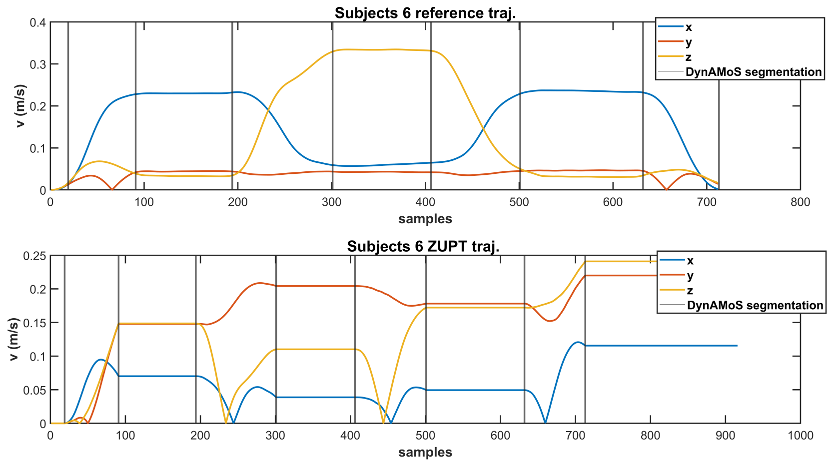

(b) Trajectory obtained with bad approximation of velocity profile (below) against gold standard trajectory (above).

Figure 3.25: Trajectories obtained by using a velocity profile close to Vicon as in subject 1 (a) against trajectory obtained by using a bad approximation of condition of static, as in subject 6 (b).

Chapter 4

Conclusions

This study investigates trajectory reconstruction during an R2G task using a single IMU placed on the wrist within a structured protocol. First, the inertial sensor was characterized using a custom-built workbench to evaluate its reconstruction performance in a controlled uniaxial movement, using a double integration approach, which resulted in errors on trajectory reconstruction about 6±4% of the total movement. Then, the same sensor was used to collect data from eleven healthy participants performing consecutive R2G executions.

As a final method, we propose an approach that optimizes the trajectory obtained with ZUPT by incorporating movement constraints based on the expected trajectory. This optimization minimizes a cost functional to improve trajectory reconstruction. The results were validated against a stereophotogrammetric system, used as the gold standard.

The results show that the optimization approach, using ZUPT as an initial estimate, achieves a mean absolute error distribution over time of approximately 2 ± 2 cm (corresponding to less than 10% of the full ROM) along the x-axis, where most of the movement occurs. On the other axes, the error remains below 2 ± 2 cm, corresponding to 5% of the ROM.

These findings suggest that a reconstructed trajectory closely resembling the gold standard can be achieved. However, the high number of constraints imposed may reduce accuracy when the protocol is not strictly followed. This is particularly relevant for highly motor-impaired patients, where deviations from the expected movement could lead to greater reconstruction errors. Therefore, it is crucial to ensure that the defined constraints remain feasible and using additional measures such as the monitoring of the time required for complete the task.

Additionally, the cost functional used in the optimization problem was derived from inertial data of healthy subjects. As a result, movement characteristics such as smoothness or minimal jerk may not accurately represent impaired patients movements.

A similar study on upper limb functionality using a single IMU [29], [32] demonstrated that, for a movement composed of nine sub-movements, ZUPT yielded errors of approximately 1% of the total ROM. However, the movement analyzed in that study was less complex, occurring primarily in a single direction, whereas R2G involves motion in both the transversal and sagittal planes. Moreover, the study employed an Extended Kalman Filter (EKF) for orientation estimation, which likely contributed to the error reduction. However, EKF implementation requires to define error and state covariance matrices, which are beyond the scope of this thesis.

In summary, an optimization-based method for trajectory reconstruction using a single

IMU shows promising potential for telerehabilitation due to its speed and ease of setup. However, results indicate that errors should be further reduced by refining the cost function or integrating more robust constraints to improve both accuracy and inter-subject variability. Additionally, further testing on impaired subjects, is necessary to evaluate the effectiveness of this approach in pathological movements.

Bibliography

[1] Patrick F. Edemekong, Deb L. Bomgaars, Sindhu Sukumaran, and Aditi C. Levy. *Activities of Daily Living*. StatPearls Publishing, Treasure Island (FL), updated 2023 jun 26 edition, 2023. Available from: `https://www.ncbi.nlm.nih.gov/books/NBK470404/`.

[2] Patricia F. Adams, Whitney K. Kirzinger, and Michael E. Martinez. Summary health statistics for the u.s. population: National health interview survey, 2011. *Vital and Health Statistics. Series 10, Data from the National Health Survey*, 255:1–110, Dec 2012. [PubMed].

[3] Valery L Feigin, Bo Norrving, and George A Mensah. Global burden of stroke. *Circ. Res.*, 120(3):439–448, February 2017.

[4] Eline C C van Lieshout, Ingrid G van de Port, Rick M Dijkhuizen, and Johanna M A Visser-Meily. Does upper limb strength play a prominent role in health-related quality of life in stroke patients discharged from inpatient rehabilitation? *Top. Stroke Rehabil.*, 27(7):525–533, October 2020.

[5] Alex Martino Cinnera, Pietro Picerno, Alessio Bisirri, Giacomo Koch, Giovanni Morone, and Giuseppe Vannozzi. Upper limb assessment with inertial measurement units according to the international classification of functioning in stroke: a systematic review and correlation meta-analysis. *Top. Stroke Rehabil.*, 31(1):66–85, January 2024.

[6] World Health Organization. *International Classification of Functioning, Disability and Health (ICF)*, 2001.

[7] European Commission: Joint Research Centre, M. Belmonte, S. Grubanov-Boskovic, F. Natale, A. Conte, et al. Demographic microsimulation of long-term care needs in the european union – prototype for a microsimulation model projecting the demand for long-term care up to 2070. Technical report, Publications Office of the European Union, 2023.

[8] Eurostat. Eu median age increased by 2.3 years since 2013, 2024.

[9] Eurostat. Disability statistics - elderly needs for help or assistance, 2024.

[10] Nadine Genet, Wienke GW Boerma, Dionne S Kringos, Ans Bouman, Anneke L Francke, Cecilia Fagerström, Maria Gabriella Melchiorre, Cosetta Greco, and Walter Devillé. Home care in europe: a systematic literature review. *BMC Health Services Research*, 11(1), August 2011.

[11] Krupal B Patel, Kea Turner, Amir Alishahi Tabriz, Brian D Gonzalez, Laura B Oswald, Oliver T Nguyen, Young-Rock Hong, Heather S L Jim, Anthony C Nichols, Xuefeng Wang, Edmondo Robinson, Cristina Naso, and Philippe E Spiess. Estimated indirect cost savings of using telehealth among nonelderly patients with cancer. *JAMA Netw. Open*, 6(1):e2250211, January 2023.

[12] Aditi Shivarkar. Telerehabilitation market size to hit USD 16.67 bn by 2034. `https://www.precedenceresearch.com/telerehabilitation-market`, January 2024.

[13] office of disease prevention and health promotion. https://odphp.health.gov/news/202112/physical-activity-good-mind-and-body?

[14] Hardvard medical school. https://www.health.harvard.edu/heart-health/why-you-should-move-even-just-a-little-throughout-the-day?

[15] Toufik Benmessabih, Rim Slama, Vincent Havard, and David Baudry. Online human motion analysis in industrial context: A review. *Eng. Appl. Artif. Intell.*, 131(107850):107850, May 2024.

[16] J. K. Aggarwal and Q. Cai. Human motion analysis: A review. In *Nonrigid and Articulated Motion Workshop, 1997. Proceedings., IEEE*, pages 90–102, Austin, TX, 1997. IEEE.

[17] Wikipedia contributors. Triangulation (computer vision). `https://en.wikipedia.org/wiki/Triangulation_(computer_vision)`, 2025.

[18] Bob Fisher. Camera calibration, 1997.

[19] G. Zhanshe, C. Fucheng, L. Boyu, C. Le, L. Chao, and S. Ke. Research development of silicon mems gyroscopes: a review. *Microsystem Technologies*, 21(10):2053–2066, Oct 2015.

[20] W. Niu et al. Summary of research status and application of mems accelerometers. *Journal of Computer and Communications*, 06(12):215–221, 2018.

[21] W. Viehmann. Magnetometer based on the hall effect. *Review of Scientific Instruments*, 33(5):537–539, May 1962.

[22] Alessandro Filippeschi, Norbert Schmitz, Markus Miezal, Gabriele Bleser, Emanuele Ruffaldi, and Didier Stricker. Survey of motion tracking methods based on inertial sensors: A focus on upper limb human motion. *Sensors (Basel)*, 17(6):1257, June 2017.

[23] F. Gulmammadov. Analysis, modeling and compensation of bias drift in mems inertial sensors. In *2009 4th International Conference on Recent Advances in Space Technologies (RAST)*, pages 591–596, Istanbul, Turkey, 2009.

[24] Antonio I Cuesta-Vargas, Alejandro Galán-Mercant, and Jonathan M Williams. The use of inertial sensors system for human motion analysis. *Phys. Ther. Rev.*, 15(6):462–473, December 2010.

[25] Pablo Maceira-Elvira, Traian Popa, Anne-Christine Schmid, and Friedhelm C Hummel. Wearable technology in stroke rehabilitation: towards improved diagnosis and treatment of upper-limb motor impairment. *J. Neuroeng. Rehabil.*, 16(1):142, November 2019.

[26] Thorsten Meyer, Christoph Gutenbrunner, Jerome Bickenbach, Alarcos Cieza, John Melvin, and Gerold Stucki. Towards a conceptual description of rehabilitation as a health strategy. *J. Rehabil. Med.*, 43(9):765–769, September 2011.

[27] V Mathiowetz, G Volland, N Kashman, and K Weber. Adult norms for the box and block test of manual dexterity. *Am. J. Occup. Ther.*, 39(6):386–391, June 1985.

[28] Isaac Skog, Peter Händel, John-Olof Nilsson, and Jouni Rantakokko. Zero-velocity detection — an algorithm evaluation. *IEEE Trans. Biomed. Eng.*, 57(11):2657–2666, November 2010.

[29] Lu Bai, Matthew G Pepper, Yong Yan, Sarah K Spurgeon, Mohamed Sakel, and Malcolm Phillips. Quantitative assessment of upper limb motion in neurorehabilitation utilizing inertial sensors. *IEEE Trans. Neural Syst. Rehabil. Eng.*, 23(2):232–243, March 2015.

[30] Shahid Ayub, Xiaowei Zhou, Soroush Honary, Alireza Bahraminasab, and Bahram Honary. Indoor pedestrian displacement estimation using smart phone inertial sensors. *Int. J. Innov. Comput. Appl.*, 4(1):35, 2012.

[31] Risang Yudanto, Agusmian P Ompusunggu, and Abdellatif Bey-Temsamani. On improving low-cost IMU performance for online trajectory estimation. In José Luis Sánchez-Rojas and Riccardo Brama, editors, *Smart Sensors, Actuators, and MEMS VII; and Cyber Physical Systems*. SPIE, May 2015.

[32] Lu Bai, Matthew G. Pepper, Zhibao Wang, Maurice D. Mulvenna, Raymond R. Bond, Dewar Finlay, and Huiru Zheng. Upper limb position tracking with a single inertial sensor using dead reckoning method with drift correction techniques. *Sensors*, 23(1):360, December 2022.

[33] M. Caruso, E. Digo, L. Gastaldi, S. Pastorelli, and A. Cereatti. A constrained-based optimization method for real-time kinematics using magneto-inertial signals: Application to upper limb joint angles estimation during prolonged recordings. *IEEE Access*, 12:115615–115627, 2024.

[34] S O H Madgwick, A J L Harrison, and R Vaidyanathan. Estimation of IMU and MARG orientation using a gradient descent algorithm. In *2011 IEEE International Conference on Rehabilitation Robotics*. IEEE, June 2011.

[35] Marco Caruso, Angelo Maria Sabatini, Daniel Laidig, Thomas Seel, Marco Knaflitz, Ugo Della Croce, and Andrea Cereatti. Analysis of the accuracy of ten algorithms for orientation estimation using inertial and magnetic sensing under optimal conditions: One size does not fit all. *Sensors*, 21(7):2543, April 2021.

[36] Sara Stančin and Sašo Tomažič. Time- and computation-efficient calibration of MEMS 3D accelerometers and gyroscopes. *Sensors (Basel)*, 14(8):14885–14915, August 2014.

[37] Vicon Motion Systems. Vicon tracker 2 manual, n.d.

[38] Julien Chardonnens, Julien Favre, and Kamiar Aminian. An effortless procedure to align the local frame of an inertial measurement unit to the local frame of another motion capture system. *J. Biomech.*, 45(13):2297–2300, August 2012.

[39] Elena Bergamini, Gabriele Ligorio, Aurora Summa, Giuseppe Vannozzi, Aurelio Cappozzo, and Angelo Maria Sabatini. Estimating orientation using magnetic and inertial sensors and different sensor fusion approaches: accuracy assessment in manual and locomotion tasks. *Sensors (Basel)*, 14(10):18625–18649, October 2014.

[40] Oliver J Woodman. An introduction to inertial navigation. `https://www.cl.cam.ac.uk/techreports/UCAM-CL-TR-696.pdf`.

[41] Gregorio Dotti, Marco Caruso, Daniele Fortunato, Marco Knaflitz, Andrea Cereatti, and Marco Ghislieri. A statistical approach for functional reach-to-grasp segmentation using a single inertial measurement unit. *Sensors (Basel)*, 24(18), September 2024.

[42] Roberto G Valenti, Ivan Dryanovski, and Jizhong Xiao. Keeping a good attitude: A quaternion-based orientation filter for IMUs and MARGs. *Sensors (Basel)*, 15(8):19302–19330, August 2015.

[43] Luigi Iuppariello, Giovanni D'addio, Bernardo Lanzillo, Piero Balbi, Emilio Andreozzi, Giovanni Improta, Giuliana Faiella, and Mario Cesarelli. A novel approach to estimate the upper limb reaching movement in three-dimensional space. *Inform. Med. Unlocked*, 15(100155):100155, 2019.

[44] Rene Neurauter and Johannes Gerstmayr. A novel motion-reconstruction method for inertial sensors with constraints. *Multibody Syst. Dyn.*, 57(2):181–209, 2023.